

國立交通大學
環境工程研究所
博士論文

去除奈米微粒的低壓旋風分離器

A low pressure cyclonic separator for nanoparticle removal

研究生： 陳聖傑

指導教授： 蔡春進

中華民國九十五年十二月

去除奈米微粒的低壓旋風分離器

A low pressure cyclonic separator for nanoparticle removal

研究生：陳聖傑

Student: Sheng-Chieh Chen

指導教授：蔡春進

Adviser: Chuen-Jinn Tsai

國立交通大學

環境工程研究所

博士論文



Submitted to Institute of Environmental Engineering

College of Engineering

National Chiao Tung University

in Partial Fulfillment of the Requirements

for the Degree of

Doctor of Philosophy

in Environmental Engineering

December 2006

Hsinchu, Taiwan, Republic of China

中華民國 九十五年 十二月

去除奈米微粒的低壓旋風分離器

研究生：陳聖傑

指導教授：蔡春進 博士

國立交通大學環境工程研究所

摘要

本研究設計並測試一個低壓旋風分離器來去除奈米微粒，此設備包含一個臨界流孔板和連接於其下游的一個軸向旋風器，臨界流孔板用於降低旋風器的壓力，使微粒滑動校正係數提高、阻力降低，進而提升旋風器對奈米微粒的收集效率。

由於微粒通過流孔板時可能會損失在其中，所以本研究探討微粒流經流孔板時的損失情形，並研究減少損失的方法。本研究探討的流孔板為 O'Keefe 公司的 E-9 流孔板(O'Keefe Control Co.)，其孔徑為 0.231 mm，上下游各接有入口管(內徑 10.4 mm, 長度 90 mm)和出口管(內徑 6.2 mm, 長度 60 mm)，臨界流量為 0.455 slpm。當上游壓力為 760 Torr，下游為 260 Torr 時，奈米微粒(氣動直徑小於 100 奈米)於流孔板內的擴散損失很小，粒徑 15 奈米時僅為 3.4%，慣性衝擊損失也接近於零。當下游壓力降低至 5.4 Torr 時，奈米微粒擴散損失仍很小，但慣性衝擊損失會高達 50%，主要發生在流孔板下游管壁上，解決方法為加大下游管徑，如將下游管徑從 6.2 mm 增加至 25 mm，則奈米微粒慣性衝擊損失會降為零。

本研究的軸向旋風器有一個旋轉三圈的導翼片，其內徑為 15 mm，中心軸半徑為 10 mm。實驗時的旋風器進口壓力為 4.3~7 Torr，流量為 0.351~0.566 slpm，測試微粒為固體氯化鈉和液體油酸微粒，直徑 12~100 奈米。結果顯示當流量固定，旋風器的效率會隨進口壓力降低而增加，如流量為 0.455slpm 時，當旋風器進口壓力從 6.0 Torr 降為 5.4 Torr，旋風器對油酸和氯化鈉微粒的截取氣動直徑分別會從 49.8 和 47.1 奈米減少為 23.1 和 21.2 奈米。此外本研究發現氯化鈉和油酸微粒有相近的收集效率，所以固體微粒在此旋風器內的彈跳問題幾乎不存在。

以三維數值模擬方法計算旋風器的流場，發現在導翼片內的切線速度分布近似拋物面，根據這個發現，本研究推導出旋風器的收集效率的理論值，其結果與實驗數據符合，最大誤差在 15% 以內。本研究也推出一個可預測不同旋風器壓力及操作流量下旋風器截取氣動直徑的半經驗公式，此公式可準確預測截取氣動直徑，誤差在 9% 以內，根據此半經驗公式，我們算得半經驗的截取史托克數平方根 $\sqrt{St_{50}^*}$ 為 0.241 的常數值。

上述的理論收集效率僅考慮導翼片中微粒受離心力之去除作用，未考慮到導翼片下游腔體中的微粒去除，且沒有考慮到細微粒的擴散作用，因此誤差較大。為進一步準確計算旋風器的微粒收集效率，本研究先以三維數值模擬求得旋風器內全部的流場，再運用布朗尼動力模擬方法進行微粒收集效率的計算，同時考慮微粒受離心力及擴散作用的影響。結果顯示在不同操作條件下，旋風器的收集效率和截取粒徑都和實驗數據相當接近，最大誤差在 3.5% 以內。此外發現微粒的擴散損失主要發生於導翼片之後的微粒收集腔體中，因為氣流出了導翼片之後速度大幅降低，微粒因而有較長的停留時間由於擴散作用而被收集。

本研究的低壓旋風分離器可有效去除奈米微粒，推導出的旋風器截取氣動直徑半經驗公式和布朗尼動力模擬的結果，可設計低壓旋風分離器用於篩選某粒徑以下的奈米粉體、去除高科技製程反應腔真空排氣中的有毒微粒、及作為奈米微粒的採樣之用。

A low pressure cyclonic separator for nanoparticle removal

Student: Sheng-Chieh Chen

Adviser: Dr. Chuen-Jinn Tsai

Institute of Environmental Engineering

National Chiao Tung University

ABSTRACT

In this study, a low pressure cyclonic separator for nanoparticle removal was designed and tested. The device included a critical orifice and an axial flow cyclone connected downstream of the orifice. The orifice was used to reduce the pressure of the cyclone. At reduced pressure, particle slip correction factor is increased and particle drag force decreased by a significant amount resulting in an increasing collection efficiency of nanoparticles.

Particle loss may occur as particles pass through the orifice. Therefore, this study investigated particle loss in the orifice and the method to reduce the loss at first. The investigated orifice was the O'Keefe E-9 (O'Keefe Control Co.) orifice whose inner diameter was 0.231 mm and critical flow rate was 0.455 slpm. At the upstream and downstream of the orifice, there is an inlet tube (inner diameter=10.4 mm, length=90 mm) and outlet tube (inner diameter=6.2 mm, length=60 mm), respectively. As the upstream pressure (P_{ou}) and downstream pressure (P_{od}) of the orifice was 760 Torr and 260 Torr, respectively, nanoparticle (smaller than 100 nm in aerodynamic diameter) diffusion loss in the orifice was found to be very low and impaction loss was nearly zero. Diffusion deposition loss was only 3.5% for 15 nm particles. When P_{od} was reduced to 5.4 Torr, nanoparticle diffusion loss was still low however inertial impaction loss was increased to 50%, which mainly occurs at the tube wall downstream of the orifice. Increasing the inner diameter of the outlet tube was found to reduce particle loss due to inertial impaction. For example, increasing inner diameter from 6.2

mm to 25 mm, particle loss was reduced to zero.

The axial flow cyclone tested in the present study has one vane which makes three complete turns. The inner radius of the cyclone was 15 mm and the radius of the spindle was 10 mm. In the experiment, the operated pressures at cyclone inlet (P_{in} or P_{od}) and the flow rates were ranged from 4.3 to 7 Torr and 0.351 to 0.566 slpm, respectively. Liquid OA (oleic acid) and solid NaCl particles in size between 12 and 100 nm were used to examine the collection efficiency of the cyclone. Results showed that at a fixed flow rate, particle collection efficiency of the cyclone was increased with decreasing P_{in} . For example, when the flow rate was fixed at 0.455 slpm, the cutoff aerodynamic diameters of OA and NaCl were reduced from 49.8 and 47.1 to 23.1 and 21.2 nm, respectively as P_{in} was reduced from 6 to 5.4 Torr. In addition, it was found the collection efficiencies of NaCl and OA particles were close to each other in the size range from 25 to 180 nm in aerodynamic diameter. This is to say the effect of solid particle bounce on collection efficiency does not exist in the cyclone.

Using 3-D numerical simulation to calculate the flow field of the axial flow cyclone, it was found the tangential flow velocity distribution in the vane section was paraboloid. Based on this finding, theoretical equation for particle collection efficiency of the cyclone was derived and showed good agreement with the experimental data with the maximum error of 15%. A semi-empirical equation for predicting the cutoff aerodynamic diameter at different inlet pressures and flow rates was also obtained. The semi-empirical equation is able to predict the cutoff aerodynamic diameter accurately within 9 % of error. From the empirical cutoff aerodynamic diameter, a semi-empirical square root of the cutoff Stokes number, $\sqrt{St_{50}^*}$, was calculated and found to be a constant value of 0.241.

The above theoretical collection efficiency only considered particle centrifugal force in the vane section, without considering particle removal in the chamber downstream of the vane. Also the diffusional effect of fine particles was not included. These all led to errors in

theoretical collection efficiency. In order to improve the accuracy of particle collection efficiency, 3-D numerical simulation was conducted to obtain the total flow field first. Then Brownian Dynamic (BD) simulation was applied to calculate particle collection efficiency considering both particle centrifugal and diffusional effects. The simulated results of both particle collection efficiency and cutoff aerodynamic diameter are in good agreement with the experimental data with the maximum derivation of less than 3.5% at different operating conditions. The increase in the diffusional deposition was found to occur mainly in the chamber after the vane section when the gas expands and slows down. Therefore, particles have longer residence time to be collected in the chamber by diffusion.

The low pressure cyclonic separator developed in this study can remove nanoparticles efficiently. The derived semi-empirical equation of cutoff aerodynamic diameter and the results of BD simulation can facilitate the design of the low pressure cyclonic separator to classify nanopowders below a certain diameter, to remove toxic nanoparticles from the vacuum exhaust of process chambers commonly used in high-tech industries, and can be used for nanoparticle sampling.

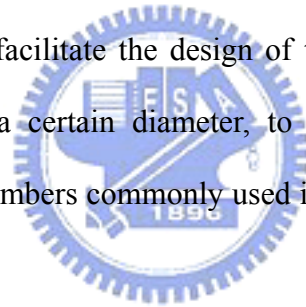


TABLE OF CONTENTS

ABSTRACT (Chinese)	I
ABSTRACT (English)	III
ACKNOWLEDGEMENTS	VI
TABLE OF CONTENTS	VII
LIST OF TABLES	IX
LIST OF FIGURES	X
LIST OF SYMBOLS	XII
CHAPTER 1 INTRODUCTION.....	1
1.1 Motivation	1
1.2 Objective.....	2
1.3 Content of this thesis	4
CHAPTER 2 LITERATURE REVIEW	7
2.1 Particle loss in a critical orifice	7
2.2 Particle collection efficiency of cyclones.....	13
CHAPTER 3 METHODS	18
3.1 Experimental method	18
3.1.1 Particle loss of the critical orifice assembly.....	18
3.1.2 Particle collection efficiency of the axial flow cyclone	23
3.2 Theoretical method for particle collection efficiency of the axial flow cyclone .	27
3.3 Numerical method	29
3.3.1 Flow field of the critical orifice assembly	29
3.3.2 Particle loss in the critical orifice assembly.....	29
3.3.3 Particle collection efficiency of the axial flow cyclone	36
3.3.4 Brownian Dynamic simulation of particle collection efficiency.....	38
CHAPTER4 RESULTS AND DISCUSSION.....	44
4.1 Particle loss in the critical orifice assembly.....	44
4.1.1 Diffusion loss	44
4.1.2 Inertial impaction loss on the front surface of the orifice	45
4.1.3 Inertial impaction loss in the downstream tube of the orifice.....	49

4.1.4 Particle loss at different parts of the orifice.....	50
4.2 Particle collection efficiency of the axial flow cyclone.....	56
4.2.1 Comparison of liquid and solid particles	56
4.2.2 Solid particle loading effect	56
4.2.3 Collection efficiency of OA particles at different operating conditions.....	60
4.3 Numerical results for flow field and particle collection efficiency of the cyclone	62
4.3.1 Simulated flow and pressure fields	62
4.3.2 Semi-empirical equation of cutoff aerodynamic diameter	69
4.4 Results of Brownian Dynamic simulation for particle collection efficiency.....	75
4.4.1 Comparison of simulated collection efficiency with present experimental data.....	75
4.4.2 Comparison of simulated collection efficiency with the results of Hus et al. (2005).....	80
CHAPTER 5 CONCLUSIONS AND RECOMMENDATIONS	83
5.1 Conclusions.....	83
5.2 Recommendations.....	85
REFERENCES	87
VITA	92
PUBLICATION LIST	93

LIST OF TABLES

Table 4.1 Comparison of $SQRT(St')$ and particle loss in the TAO for different outlet tube diameters, $P_{od}=260$ Torr.....	52
Table 4.2 Comparison of $SQRT(St')$ and particle loss in the TAO for different outlet tube diameters, $P_{od}=5.4$ Torr.....	55
Table 4.3 Cutoff aerodynamic diameter at different operating conditions, liquid oleic acid (OA) particles.....	72
Table 4.4 Cutoff aerodynamic diameter for different operating conditions.	77



LIST OF FIGURES

Figure 1.1 Schematic diagram of a local scrubber in semiconductor industry.....	5
Figure 1.2 Schematic diagram of the low pressure cyclonic separator	6
Figure 2.1 Schematic diagrams of the orifice assembly. (a) Locations of particle loss, (b) 2-D view of the computational domain.....	12
Figure 3.1 Experimental setup for measuring loss of small particle (<1 μm).....	20
Figure 3.2 Experimental setup for measuring loss of larger particle (2-15 μm).....	22
Figure 3.3 Experimental setup for testing collection efficiency of the cyclone.	24
Figure 3.4 Schematic diagrams of the spindle and vane design	26
Figure 3.5 Schematic diagram of a tetrahedral cell.	33
Figure 3.6 Critical particle radial positions and collection regions at the entry plane of the inlet tube. (OP: orifice plate; TAO: tube after orifice)	35
Figure 4.1 Comparison of simulated diffusional deposition efficiencies with experimental data.	47
Figure 4.2 Particle deposition efficiency on the front surface of the orifice.....	48
Figure 4.3 Particle deposition efficiency on the tube after the orifice.	51
Figure 4.4 Particle deposition efficiency on different parts of the orifice assembly.....	54
Figure 4.5 Particle collection efficiency versus aerodynamic diameter for solid NaCl and liquid OA particles at different inlet pressures.....	58
Figure 4.6 Particle loading effect on collection efficiency, solid NaCl particles.....	59
Figure 4.7 Particle collection efficiency versus aerodynamic diameter for OA particles at different inlet pressures and flow rates.....	61
Figure 4.8 Maximum tangential velocity and pressure distribution in the vane, numerical results.....	63
Figure 4.9 Tangential velocity profile at the cutting plane of the vane section, the end of (a) 2 turns (2-D), (b) 3 turns (2-D) and (c) 3 turns (3-D).....	64
Figure 4.10 Critical curves at the entry plane of the first segment for particle collection.....	67
Figure 4.11 Comparison of numerical collection efficiencies and experimental data.....	68
Figure 4.12 Collection efficiencies versus $\sqrt{St/St_{50}}$ for OA particles at different inlet	

pressures and flow rates.....	73
Figure 4.13 Comparison of numerical collection efficiencies and present experimental data, (a) $P_{in}=6.0$ Torr; (b) $P_{in}=7.0$ Torr.....	78
Figure 4.14 Comparison of numerical collection efficiencies and present experimental data, $P_{in}=4.3, 5.4, 6.8$ torr.	79
Figure 4.15 Comparison of the present numerical collection efficiencies with the experimental data and the theory by Hsu et al. (2005)	82

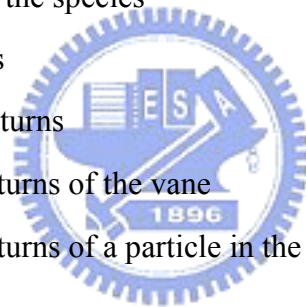


LIST OF SYMBOLS

English Symbols

A	a parameter
A_c	collection area
A_i	inlet area of the orifice assembly
A_o	orifice area
B	pitch of vane
C	mass concentration of nanoparticles
C_c	Cunningham slip correction factor
C_D	drag coefficient
C_d	particle concentration of the orifice downstream
C_u	particle concentration of the orifice upstream
D_i	inlet tube diameter of the orifice assembly
D_o	orifice diameter
D_{out}	inner diameter of the outlet tube of the cyclone
D_p	particle diameter
D_{pa}	aerodynamic diameter
D_{pa50}	cutoff aerodynamic diameter
$D_{pa,cent}$	centrifugal cutoff aerodynamic diameter
$D_{pa,diff}$	diffusional cutoff aerodynamic diameter
dr	differential radial migration distance of particle
D_s	diffusivity of the species
D_t	tube inner diameter after the orifice
F	a variable
$F^{(B)}$	random force resulting from the particle bombardment by gas molecules
$F^{(D)}$	drag force on the particle
$F^{(ext)}$	external force
g	gravitational acceleration

G_{Li}	a random number
G_{Vi}	a random number
H	a dimensionless variable
H_l	modified Stokes number
J	mass flux
K	an empirical factor
k_B	Boltzmann's constant
K_n	Knudsen number
L	effective body length
L_{min}	minimum length of the cells adjacent to the particle's present cell
M	equation of Chandrasekhar's first lemma
m	particle mass
m_s	mass fraction of the species
N	number of vanes
n	number of vane turns
n_T	total number of turns of the vane
$n\zeta$	total number of turns of a particle in the cyclone
P_{760}	760 Torr
P_{cyc}	average pressure of cyclone inlet and outlet
P_{en}	overall particle penetration of the axial flow cyclone
P_{in}	inlet pressure of the cyclone
P_n	pressure at n^{th} turn of the vane
P_{od}	downstream pressure of the orifice
P_{ou}	upstream pressure of the orifice
P_{out}	outlet pressure of the cyclone
Q	gas volumetric flow rate
Q_0	standard gas volumetric flow rate
R	contraction ratio
Re	Reynolds number
Re_p	particle Reynolds number



r_{max}	inner radius of the cyclone
r_{min}	radius of the vane spindle
r_o	inlet tube radius of the orifice assembly
r_{OP}	critical particle radial position of collection region OP
r_{TAO}	critical particle radial position of collection region TAO
s	species
St	Stokes number
St'	modified Stokes number relative to U_o and D_t
St_{50}	Stokes number corresponding to 50% deposition (or collection) efficiency
St_{50}^*	semi-empirical cutoff Stokes number
St_b	Stokes number of the axial flow cyclone
St_o	Stokes number based on U_i and D_o
T	absolute temperature
t_v	transit time of a particle in the vane section
U	flow velocity
U_a	mean axial gas velocity in the body section of the cyclone
U_i	average velocity at the inlet tube of the orifice
U_{max}	maximum flow velocity of the cells adjacent to particle's present cell
U_o	average flow velocity at the orifice
V	particle velocity
V_a	mean gas velocity in the vane section of the cyclone
V_r	particle radial velocity
Vol	effective volume in the vane section
$V_{t,n^{th}}(r,z)$	tangential velocity of the entry plane of the n^{th} segment at position (r,z)
\bar{V}_a	average axial velocity
\bar{V}_t	average tangential gas velocity in the vane section

$\bar{V}_{t,1}$	average tangential gas velocity at the entry plane of the 1 st segment of the vane section
$\bar{V}_{t,n^{th}}$	average tangential gas velocity at the entry plane of the n th segment of the vane section
$\bar{V}'_{t,1}$	average tangential gas velocity at the first segment of the collection area
w	vane thickness
x, y, z	Cartesian coordinate

Greek symbols

Δr	total particle radial migration distance
ΔL_i	particle linear displacement
Δt	time step of each iteration
ΔV_i	change of particle velocity
$\langle \Delta L_i \rangle$	expected values of particle displacement in the i-th direction
$\langle \Delta V_i \rangle$	expected values of particle velocity change in the i-th direction
F	a factor, defined as V_a/U_a
α, β, γ	fractions of the difference vectors $\overline{P1P4}$, $\overline{P1P2}$ and $\overline{P1P3}$, respectively
η_{Dpa}	collection efficiency of D_{pa} particle
η_o	particle deposition efficiency in the orifice assembly
η_{OP}	deposition efficiency of particles at OP
η_{TAO}	deposition efficiency of particles at TAO
$\varphi(M)$	probability distribution of M
$\varphi_i(\Delta V_i, \Delta L_i)$	bivariate normal density probability distribution function
λ	mean free path of the air molecules
λ_0	mean free path of the air molecules at standard condition
μ	air dynamic viscosity
θ	contraction half-angle
ρ	air density

ρ_c	a coefficient of correlation
ρ_p	particle density
ρ_{p0}	unit density
σ_{Li}	standard deviations of displacement
σ_{Vi}	standard deviations of particle velocity change
τ	particle relaxation time
$\bar{\tau}_{nth}$	average relaxation time of particle
$\psi(\xi)$	any function of time, varying much slower than the fluctuating Brownian force



CHAPTER 1

INTRODUCTION

1.1 Motivation

Many toxic gas pollutants (SiH_4 , TEOS, SiH_2Cl_2 , SiCl_4 , etc.) (McMahon, 1989) as well as fine particles (SiO_2 and metallic particles, such as As oxide) are emitted from the reaction chambers of semiconductor and photo-electronic industries. Residual gases are usually treated by local scrubbers located behind a vacuum pump with high efficiency (Blachman and Lippmann, 1974), as shown in Fig. 1.1. However, local scrubbers are not efficient for fine particle removal (Librizzi and Manna, 1983). Particles can deposit on the tube wall after the reaction chamber or in between the vacuum pump and local scrubber. Once particles accumulate to a significant amount, they can clog up the tube resulting in process intervention or explosion hazard. Furthermore, fine particles emitted from the local scrubber are not treated efficiently by the central scrubber either.

Between the reaction chamber and the vacuum pump, pressure is very low, typically less than several Torr. It is desirable to have a particle control device which works at this condition. Otherwise particles have to be removed at ambient pressure by a baghouse or an electrostatic precipitator, which is costly and occupies too much space to use in the high-tech industry. If the pressure is reduced below several Torr, particle drag force will be reduced by a significant amount and then it is possible to use a cyclone to remove fine particles by centrifugal force. An axial flow cyclone is such a good candidate. Additional advantage is that the axial flow cyclone can be installed in line with the flow direction.

To determine size distribution of nanoparticle in ambient air, inertial impactors such as the low pressure cascade impactor developed by Vanderpool et al. (1990) and the nano-MOUDI by commercialized MSP Co. are normally used. However, previous studies (Tsai and

Cheng, 1995; Tsai and Lin, 2000; Biswas and Flagan, 1988) showed that solid particles can bounce easily from the impaction substrate. In contrast, solid particle bounce in a cyclone is less a problem. Therefore it is desirable to develop a low pressure axial flow cyclone for nanoparticle sampling.

The objective of this study is to design and test an axial flow cyclone operated at reduced pressure. In case nanoparticles to be removed or sampled are suspended in ambient condition, a pressure reducing device has to be installed in front of the cyclone. In this study, a critical orifice was used to reduce the pressure of the cyclone. The schematic diagram of the low pressure cyclonic separator for removing nanoparticles is shown in Fig. 1.2, in which particles are suspended at ambient condition. After passing through the orifice, the pressure of the aerosol flow is reduced to several Torr. Nanoparticles then can be removed by the downstream axial flow cyclone.

1.2 Objective

In order to reduce the pressure in the cyclone, commercial critical orifices (O'Keefe Controls Co., type E-8, E-9 and E-10) were installed at the upstream of the cyclone. Because the diameter of the orifice is very small, particle loss may occur in the orifice and eventually clog it up. Therefore, particle loss in the orifice must be reduced.

Orifices are widely used to control flow rate, or use as a pressure reducing device for high purity gas sampling (Lee et al., 1993), or used in a particle focusing apparatus (Liu et al., 1995; Lee et al., 2003; Das and Phares, 2004). In these applications, it is desirable to have particle loss in the orifice as minimum as possible.

Previous works on axial flow cyclones include the experimental studies of Liu and Rubow (1984), Weiss et al. (1987) and Vaughan (1988), and the theoretical study of Maynard (2000). In these studies, axial flow cyclones were tested in ambient conditions. Until now, no researchers have ever investigated the collection efficiency of an axial flow cyclone in

reduced pressure conditions.

In the previous study of Tsai et al. (2004), a theoretical equation was derived to predict the cutoff aerodynamic diameter of an axial flow cyclone. They found the theoretical cutoff diameter had to be adjusted by the flow Reynolds number to fit the experimental data. The reason why there is such as a discrepancy has yet to be found.

Brownian Dynamic (BD) simulation was successfully applied to calculate the single fiber efficiency in which both inertial impaction and Brownian diffusion were taken into account (Ramarao et al., 1994). If BD simulation can be used to calculate the particle collection efficiency of the axial flow cyclone, both centrifugal force and Brownian diffusion can be taken into account. It is expected to be more accurate than the theoretical equation of Tsai et al. (2004) in which the Brownian diffusion effect on collection efficiency was not considered.

The objectives of this study are summarized below:

1. To use both numerical and experimental methods to study particle deposition efficiency at different parts of the orifice assembly and find out a best geometry of the orifice assembly to reduce particle loss.
2. To test and compare the collection efficiency of the axial flow cyclone for both liquid (OA) and solid (NaCl) nanoparticles and to examine the solid particle loading effect on collection efficiency.
3. To calculate the flow and pressure fields and the particle efficiency of the cyclone using a 3-D numerical method and BD simulation.
4. To compare experimental collection efficiencies with theoretical results obtained using simulated flow and pressure fields and numerical results by BD simulation.
5. To develop a semi-empirical equation to predict the cutoff aerodynamic diameter of the axial flow cyclone.

1.3 Content of this thesis

In chapter 2, previous studies on particle loss in a critical orifice are reviewed. Then the experimental and theoretical works on the collection efficiency of tangential or axial flow cyclones in the literature are also reviewed.

In chapter 3, experimental methods for determining particle loss in the critical orifice and particle collection efficiency of the axial cyclone are first described. Then a theoretical method for calculating the particle collection efficiency of the cyclone is introduced. After the theoretical method, numerical methods for calculating the flow field and the particle loss of the orifice are presented. Next is the numerical method for calculating the flow field and the collection efficiency of the cyclone. Finally, BD simulation is introduced which calculates nanoparticle collection efficiency considering both centrifugal force and Brownian diffusion simultaneously.

In chapter 4, particle loss at different parts of the orifice and the comparison of present experimental data and numerical results are shown. Then the experimental data for particle collection efficiency of the axial cyclone are presented. The experimental data and the numerical results of particle collection efficiency are compared. At last, the results of BD simulation for particle collection efficiency are compared with the present data and the results of Hus et al. (2005).

In chapter 5, conclusions of this thesis are summarized and recommendations are suggested.

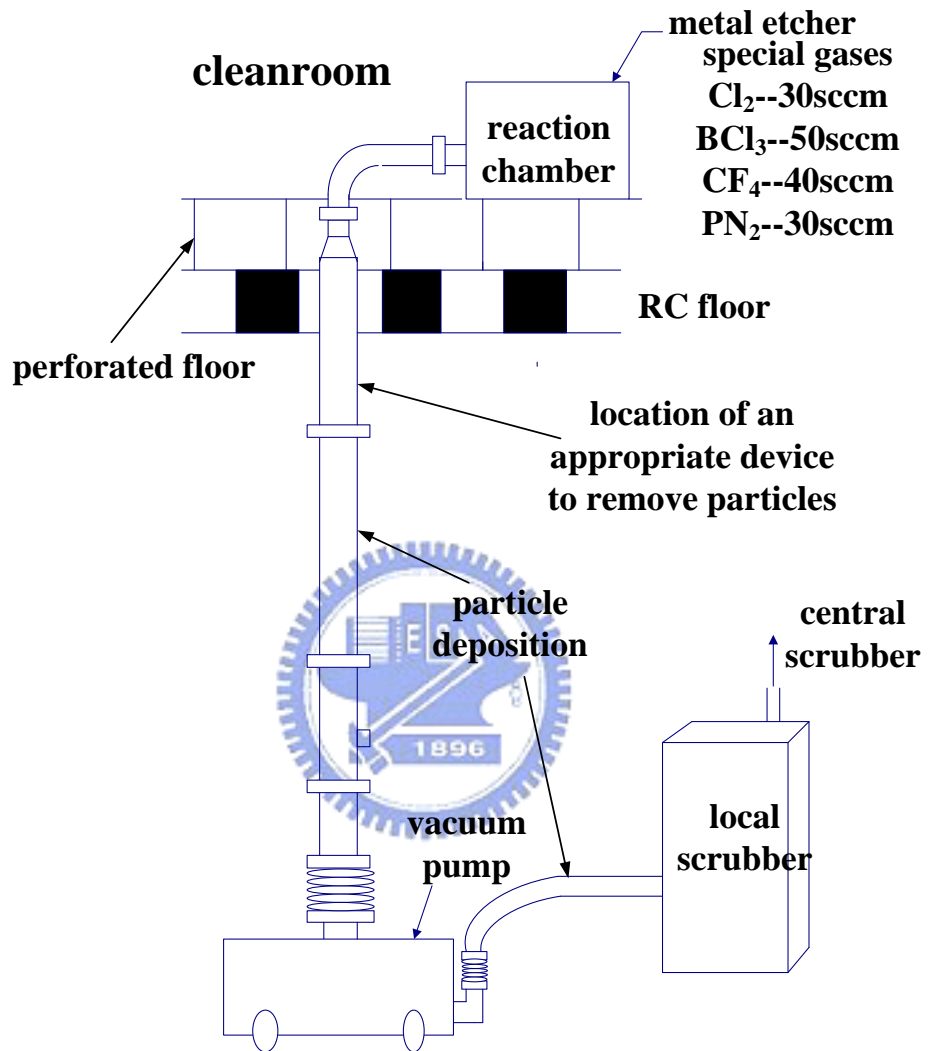


Figure 1.1 Schematic diagram of a local scrubber in semiconductor industry.

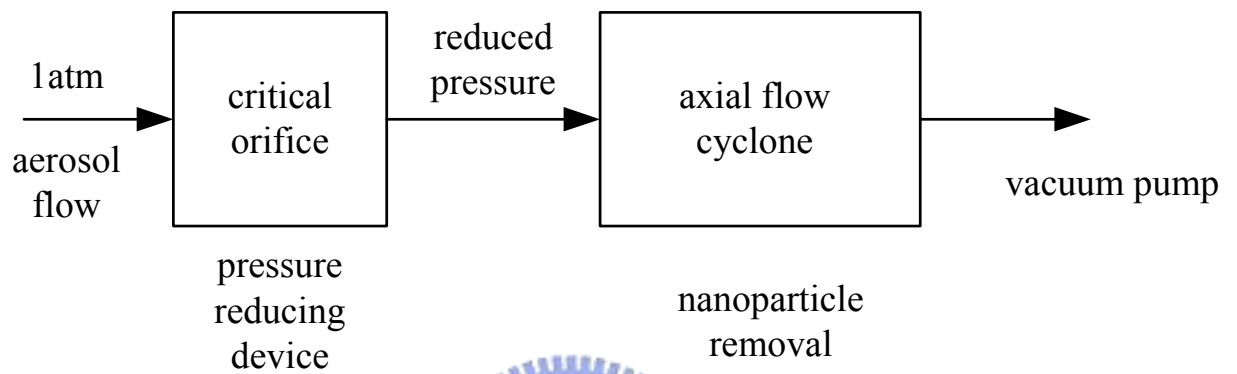
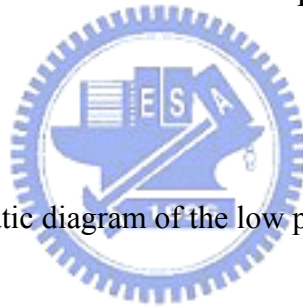


Figure 1.2 Schematic diagram of the low pressure cyclonic separator



CHAPTER 2

LITERATURE REVIEW

2.1 Particle loss in a critical orifice

Orifices are widely used to control flow rate. In this study, commercial critical orifices (O'Keefe Controls Co., type E-8, E-9 and E-10) were installed at the upstream of the cyclone to reduce pressure in the cyclone. Because the diameter of the orifice is very small, particle loss may occur in the orifice and eventually clog it up. Therefore, particle loss in the orifice must be reduced.

The critical orifice was used as a pressure reducing device for high purity gas sampling by Lee et al. (1993). In this case it is important to avoid particle loss in the orifice so that particle concentration in the pipe flow can be measured accurately. Lee et al. (1993) reviewed particle deposition mechanisms in orifice-type pressure reducers including inertial impaction at the front side and the back side of the orifice, and on the chamber (or tube) wall downstream of the orifice. They also illustrated that the loss of nanoparticles (<100 nm) can also occur due to diffusional mechanism. The schematic diagram of the critical orifice assembly and the deposition regions of particles are shown in Fig. 2.1.

The deposition loss due to particle inertial impaction on the front surface of the orifice was studied by Ye and Pui (1990) for an abrupt contraction with a contraction half-angle, θ of 90° . Assuming the air flow is laminar and fully developed, they obtained an empirical equation of the deposition efficiency, η_o , as

$$\eta_o = 1 - \exp(1.721 - 8.557F + 2.227F^2) \quad (2.1)$$

where the variable F and the contraction ratio R are defined as

$$F = \sqrt{St_o} / (R)^{0.31} \quad (2.2)$$

$$R = D_i / D_o \quad (2.3)$$

In above equations, D_o is the orifice diameter, D_i is the inner diameter of the inlet tube and St_o is the Stokes number which is defined as

$$St_o = \frac{\rho_p D_p^2 U_i C_c}{9\mu D_o} \quad (2.4)$$

where U_i (m/s) is the average velocity at the inlet tube, D_p (m) is the particle diameter, ρ_p (kg/m^3) is the particle density, C_c is the Cunningham slip correction factor and μ is the air dynamic viscosity. In their study, the contraction ratio R was in the range of 2-10 and the Reynolds number was in the range of 100-200, which was based on the inlet tube diameter (D_i) and the average velocity at the inlet tube (U_i). Chen and Pui (1995) extended the work of Ye and Pui (1990) further to consider the effect of different θ (15° to 90°) on the inertial particle deposition efficiency. The Reynolds number was fixed at 1000 while the R was varied from 2.0 to 5.0. The results of the deposition efficiency for $\theta > 75^\circ$ were found to be the same as those in Ye and Pui (1990).

For $\theta < 60^\circ$, the following empirical equation for the deposition efficiency on the front side of the orifice was obtained:

$$\eta = [0.882 + 0.0272H^{0.5} - 8.272H^{0.5} \exp(-3.627H^{0.5})]^2 \quad (2.5)$$

where the dimensionless variable H is defined as

$$H = St / St_{50}, \quad (2.6)$$

St_{50} is the Stokes number corresponding to 50% deposition efficiency, which is related to the R and θ as

$$St_{50} = 0.235R^{0.61}(\sin \theta)^{-1.119} \quad (2.7)$$

Muyschondt et al. (1996) proposed that the deposition efficiency for a given contraction angle is related to the modified Stokes number as

$$\eta = \frac{1}{1 + \left[\frac{H_1}{a \exp(b\theta)} \right]^c} \quad (2.8)$$



where H_1 is the modified Stokes number, $St_o (1 - A_o/A_i)$, A_o is the orifice area and A_i is the inlet area. Constants in Eq. (2.8) were obtained from the least-square fitting of the data as $a = 3.14$, $b = -0.0185$, $c = -1.24$. Eq. (2.8) is only valid up to the limiting value of $\eta = 1 - (A_o/A_i)$ as the Stokes number becomes very large and the particles travel in a straight line.

Sato et al. (2002) investigated the particle deposition at low pressure experimentally and numerically. In their experiment, the pressure at downstream of the orifice ranged from 0.2 to 0.28 Torr, the contraction ratios R were fixed at 2, 3 and 5, and the Reynolds number based on D_i and U_i was 3. In the numerical simulation, R was also varied among 2, 3 and 5 while the flow Re was controlled at 0.1, 0.3, 3, 10 and 30. After comparing their own experimental and numerical results, the authors found the deposition efficiency could be correlated as

$$\eta = \exp(-0.5376 / H - 0.1824 / H^{7.019}) \quad (2.9)$$

In addition to the impaction loss on the front surface of the orifice, Pui et al. (1988) also found that particles could also deposit on the tube wall after the orifice. The deposition efficiency was related to another modified Stokes number, $SQRT(St')$ defined as

$$SQRT(St') = \sqrt{\frac{St_o U_o}{U_i}} (D_o / D_t)^{0.58} \quad (2.10)$$

where U_o and D_t are the average flow velocity at the orifice and the tube diameter after the orifice. The authors plotted their experimental deposition efficiency versus $SQRT(St')$ and found the data almost fell in a unique curve. From the curve, significant particle loss was found to occur as $SQRT(St') > 0.5$. Therefore, to design an expansion chamber to replace the downstream tube and keep $SQRT(St') < 0.1$ is necessary to reduce particle loss.

Orifices are also used in a particle focusing apparatus, called aerodynamic lenses, to form nanoparticle beams (Liu et al., 1995; Lee et al., 2003; Das and Phares, 2004). Narrow particle beams with small divergence angles are desirable in many applications in order to achieve high transport efficiencies of particles from a sampling regime to a detector and high resolution of particle size measurements. Based on the study of Liu et al. (1995), the TSI developed the aerodynamic lens which can effectively transmit particles in the size ranges 30 to 300 nm or 100 to 3000 nm. In this device, a precision bore tube holds five thin plate orifices (aerodynamic lenses) which were mounted in sequence with spacers in between (TSI Model 3801-030 Manual). The series of apertures (orifices) can move particles closer to the center axis after passing each individual aperture if their aerodynamic sizes are less than a critical value.

Another study on particle focusing was conducted theoretically at atmospheric pressure by Lee et al. (2003) and verified by the particle beam size measured by laser light scattering. The results showed that a strongly focused particle beam was obtainable with a single orifice at atmospheric pressure when the orifice Reynolds number was in the range of $300 \leq Re \leq 700$, which was based on D_o and U_o .

In the application of orifices for aerodynamic lenses, it is also desirable to have particle loss in the orifices as minimum as possible.



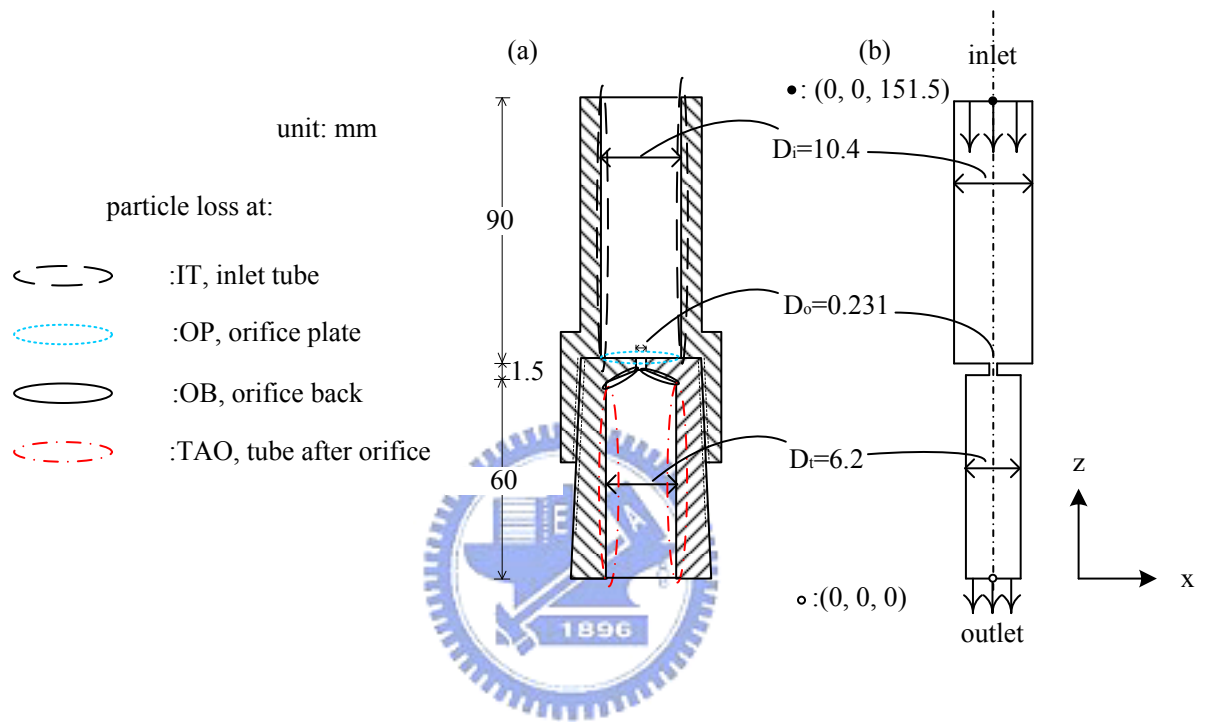


Figure 2.1 Schematic diagrams of the orifice assembly. (a) Locations of particle loss, (b) 2-D view of the computational domain.

2.2 Particle collection efficiency of cyclones

Cyclones are normally used to remove particles larger than 5-10 μm in aerodynamic diameter. To reduce the cutoff diameter, the cyclone diameter must be reduced or the flow rate must be increased. For example, Zhu and Lee (1999) tested a small tangential cyclone (cyclone diameter, $D=3.05\text{ cm}$) and found the cutoff size to be $0.3\ \mu\text{m}$ when it was operated at 110 slpm. For axial flow cyclones, Liu and Rubow (1984), Weiss et al. (1987) and Vaughan (1988) studied the axial flow cyclone operating at ambient condition. For example, Liu and Rubow (1984) developed an axial flow cascade cyclone at a design flow rate of 30 L/min for sampling high concentration of particles. The cutoff aerodynamic diameter of the five stages are 12.2, 7.9, 3.6, 2.05 and $1.05\ \mu\text{m}$. Total particle loss in the system, including the loss in the body, vane insert and exit tube of the collection cup, was shown to be significant. It ranged from 15 % for particles of $1\ \mu\text{m}$ in diameter to 33.3 % for particles of $8\ \mu\text{m}$ in diameter. Therefore, using this cascade cyclone to measure particle size distributions requires complete recovery of all particles lost in the cyclone.

Different materials of particles may result in different collection efficiencies. For impactors, it is well-known that the collection of liquid particles is better than that of solid particles due to solid particles bounce or reentrainment from the impactor substrates (Tsai and Cheng, 1995; Tsai and Lin, 2000; Biswas and Flagan, 1988). Zhu and Lee (1999) also studied the collection efficiencies differences of solid and liquid particles of a tangential flow cyclone for. Liquid dioctyl-phthalate (DOP) and solid polystyrene latex (PSL) particles in the size range of 1.0 and $3.6\ \mu\text{m}$ were found to have similar collection efficiencies even at a high flow rate of 80 slpm. However, the effect of solid particle bounce on the collection efficiency of the axial flow cyclone operating in low pressure conditions remains to be investigated.

The effect of deposited solid particles on the cyclone wall of the tangential flow cyclone has been investigated in Blachman and Lippmann (1974) and Tsai et al. (1999). The particle collection efficiency was found to increase with increasing particle mass deposited in the

cyclone (Blachman and Lippmann, 1974). Such increase is mainly due to the accumulation of dust on the cyclone wall opposite to the inlet that gradually reduces the effective diameter of the cyclone. But when the amount of deposited particles is heavy enough, the aggregated particles will be detached and then the collection efficiency will reduce again (Blachman and Lippmann, 1974). Blachman and Lippmann (1974) did not study the effect of different amounts of deposited particle mass on the collection efficiency. The solid particle loading effect on the collection efficiency for a 10 mm nylon cyclone and a new 18 mm aluminum cyclone was studied by Tsai et al. (1999). They found the cutoff aerodynamic diameter of both cyclones decreased with increasing deposited particle mass. But the 18 mm cyclone appeared to have less deposited particle mass effect on the collection efficiency due to its larger inner diameter. The cyclones tested in Blachman and Lippmann (1974) and Tsai et al. (1999) were tangential flow cyclones. There have been no studies on the solid particle loading effect on the collection efficiency for axial flow cyclones and it is expected that the axial flow cyclones will be less affected by the loaded particles on the cutoff diameter than impactors since the particle deposit in the cyclones is more diffuse.

Maynard (2000) is the first to study the particle penetration of the axial flow cyclone in ambient condition theoretically. He derived the particle penetration of the axial flow cyclone based on the assumption that particle collection mainly occurs in the vane and body sections only. The overall particle penetration, P_{en} , is combined from the penetrations derived separately for the vane and body sections as

$$P_{en} = (1 - 16\pi^2 St_b L^*)^{1/2} + \frac{4\pi^2 n^2 \Gamma^2 St_b^2}{r_{max}^{*2} - r_{min}^{*2}} - \frac{2n \Gamma St_b}{r_{max}^{*2} - r_{min}^{*2}} \left(1 + 4\pi^2 r_{min}^{*2} + 4\pi^2 \sqrt{1 - 16\pi^2 St_b L^*} \right)^{1/2} \quad (2.11)$$

where n is the number of vane turns, r_{max} is the inner radius of the cyclone (m), r_{min} is the radius of the vane spindle (m) and L is the effective body length (refer to Fig. 1 in Maynard,

2000) (m). The relative dimensions of these three variables, denoted by the variables with asterisk, is the actual dimension divided by the pitch of vanes, B (m). Stokes number St_b is defined in the body section as $St_b = \tau U_a/B$, in which τ is the particle relaxation time (sec). The factor $\Gamma = V_a/U_a$, in which V_a is the mean gas velocity in the vane section and U_a is the mean axial gas velocity in the body section. If there are N vanes and each has a finite thickness w (m), then Γ in Eq. (2.11) is calculated as

$$\Gamma = \frac{r_{\max}^* \sqrt{1 + 4\pi^2 r_{\max}^{*2}}}{2(1 - Nw^*)(r_{\max}^* - r_{\min}^*)} \quad (2.12)$$

The form of Eq. (2.12) does not allow one to obtain a simple analytical form for St_{50} (Stokes number with 50 % penetration), it must be calculated by numerical iteration. It is expected to have an analytical equation to calculate the cutoff diameter and predict the particle collection efficiency.

Tsai et al. (2004) derived an theoretical equation for predicting the cyclone cutoff aerodynamic diameter based on the air volumetric flow rate, the geometry of the cyclone, the properties of carrying gas and the pressure of the cyclone. The cutoff aerodynamic diameter D_{pa50} for the cyclone with one vane making 3 turns was derived as

$$D_{pa50} = \frac{0.106\mu(B-w)(r_{\max}^2 - r_{\min}^2)^2}{\rho_{p0}\lambda_0 r_{\min}^2 Q_0 n\zeta} \times \left(\frac{P_{cyc}}{P_{760}}\right)^2 \quad (2.13)$$

In the above equation, ρ_{p0} is unit density (1000 kg/m³), λ_0 is mean free path of air molecules at standard condition (m), Q_0 is standard volumetric flow rate (m³/sec), P_{cyc} is the average pressure of cyclone inlet and outlet (Torr), P_{760} is 760 Torr. The $n\zeta$ is the total number of turns of a particle in the cyclone, assuming that the vortex makes n turns in the vane and

additional $n(\zeta-1)$ turns downstream the vane. ζ was chosen to be 1.5 to give the best fit to the experimental data. The equation agrees well with the published experimental data on cutoff diameter (Weiss et al., 1987; Liu and Rubow, 1984; Vaughan, 1988) in ambient conditions. But at low pressure conditions (several Torr), the equation predicts the cutoff diameter much smaller than the experimental data.

Hsu et al. (2005) studied the particle collection efficiency theoretically and experimentally using the same axial flow cyclone designed in Tsai et al. (2004). They derived the equation to predict the particle collection efficiency in which both centrifugal and diffusional forces were taken into account. Plug flow assumption was made for the tangential flow in the vane section. The collection efficiency derived by Hsu et al. (2005) is

$$\eta = 1 - \exp\left[-\left(\frac{D_{pa50,diff}}{D_{pa}} + \frac{D_{pa}^2}{D_{pa50,cent}^2}\right)\right], \quad (2.14)$$


where the centrifugal cutoff aerodynamic diameter $D_{pa50,cent}$ is

$$D_{pa50} = \sqrt{\frac{9\mu(r_{max}^2 - r_{min}^2)^2 (B - Nw)^2 \ln 2}{8\pi n\zeta Q_0 r_{min}^2 N^2 BC_c}}, \quad (2.15)$$

and the diffusional cutoff aerodynamic diameter $D_{pa50,diff}$ is

$$D_{pa50,diff} = \frac{4n\zeta k_B TC_c}{3Q_0\mu \ln 2}. \quad (2.16)$$

In Eq. (2.15), k_B is the Boltzmann's constant and T is absolute temperature (K). For the flow rate of 0.455 slpm and the pressure in the cyclone of several Torr, Eq. (2.14) predicts

centrifugal force is the predominant mechanism for particle removal when particles are larger than 40 nm in aerodynamic diameter. For particles smaller than 40 nm in diameter, diffusional deposition is the main mechanism. Below 40 nm, the collection efficiency of nanoparticles increases with decreasing particle size. Experimental data presented by Hsu et al. (2005) show similar trends, but substantial disagreement exists between theoretical results and experimental data.

The flow field in the cyclone is complicated. Several researchers (Boysan et al., 1983; Hoekstra et al, 1999; Schmidt and Thiele, 2002; Harwood and Slack, 2002; Schmidt et al., 2003; Xiang and Lee, 2004) have studied the flow fields numerically for tangential flow cyclones and examined the influence of different geometries and operating conditions on the collection efficiency. Recently, Gimbut et al. (2005) used the CFD approach to simulate the particle collection efficiency of a tangential flow cyclone. In the study, in order to calculate the trajectories of particle in the flow, the discrete phase model (DPM) was used to track individual particles through the continuum fluid. The DPM model is an embedded code of the CFD program. In the model, the collection efficiency was obtained by releasing a specified number of monodisperse particles at the inlet of the cyclone and by monitoring the number escaping through the outlet. Results obtained by the authors match very well with the experimental data that were obtained by Xiang et al. (2001). However, there have been no numerical studies on the flow field and particle collection efficiency calculations with considering the both impaction and diffusion depositions of an axial flow cyclone, in particular at low pressure conditions.

CHAPTER 3

METHODS

3.1 Experimental method

3.1.1 Particle loss of the critical orifice assembly

The experimental set-up for measuring loss of small particle ($<1 \mu\text{m}$) in the orifice assembly is shown in Fig. 3.1. Polydisperse NaCl particles were generated using a constant output atomizer (TSI Model 3076) and then passed through silica gel diffusion dryer. The evaporation-condensation method using a tube furnace was employed to generate ultrafine aerosol particles. The tube furnace (Lindberg/Blue, model HTF55342C) was operated at 880°C and the residence time of aerosol particles in the furnace was 1.2 seconds. Subsequently aerosols were cooled by mixing with filtered ambient air in the mixing chamber. An impactor was used to cut particles larger than 500 nm before particles were passed through the NDMA (TSI Model 3085), which was used to classify monodisperse NaCl particles of size $15\text{-}177 \text{ nm}$ in aerodynamic diameter. The long DMA (TSI Model 3071) was used to obtain monodisperse NaCl particles of size $132\text{-}856 \text{ nm}$ in aerodynamic diameter when the impactor was not used. Then, the aerosol flow was divided into two streams, one was introduced into the orifice system and the other into the scanning mobility particle sizer SMPS (TSI model 3934). A critical orifice (E-9 O' Keefe Controls Co.) with the orifice diameter $D_o=0.0231 \text{ cm}$ and inlet diameter $D_i=1.04 \text{ cm}$ was used in the experiment (Fig. 2.1). The lengths of the inlet and outlet tubes ($D_i=0.62 \text{ cm}$) are 9 and 6 cm , respectively. The flow rate of the experiment was fixed at 0.455 slpm which corresponded to $\text{Re}=61.4$. When the flow rate was 0.455 slpm , the corresponding downstream pressure, P_{od} , was 260 Torr while the upstream pressure, P_{ou} , was fixed at 760 Torr . The flow rate of 0.455 slpm is the critical condition.

For real time measurement of total particle loss, an aerosol electrometer (AE, TSI Model

3068) was used to measure the electrical current of singly charged particles. For comparison purpose, flow rate 0.242 slpm which corresponded to $Re= 32.6$ was also tested. The corresponding downstream pressure, P_{od} , was 602 Torr while the upstream pressure, P_{ou} , was also fixed at 760 Torr. Monodisperse particles were allowed to pass through the orifice line or the by pass line alternately to measure the downstream (C_d) and upstream (C_u) aerosol concentrations. The loss was calculated as

$$loss \% = (1 - \frac{C_d}{C_u}). \quad (3.1)$$

For measuring particle loss at each part of the orifice assembly, the EA was substituted by an after filter. After introducing monodisperse NaCl particles into the orifice assembly for about 10 minutes, the assembly was disassembled and the deposited NaCl particles were wiped by using cotton swabs.

The cotton swabs were then dissolved in DI water and the solutions were analyzed by an ion chromatography (Model DX-120, Dionex Corp.). The deposition efficiency at IT, OP, OB and TAO (Fig. 2.1) can be calculated as

$$(\%) \text{ at part } i = \frac{\text{amount of } Cl^- \text{ at part "i"}}{\text{total amount of } Cl^-} \quad (3.2)$$

where “ i ” denotes the IT, OP, OB or TAO (referring to Fig. 2.1) and the total amount of Cl^- was the summation of Cl^- at IT, OP, OB, TAO and AF (after filter).

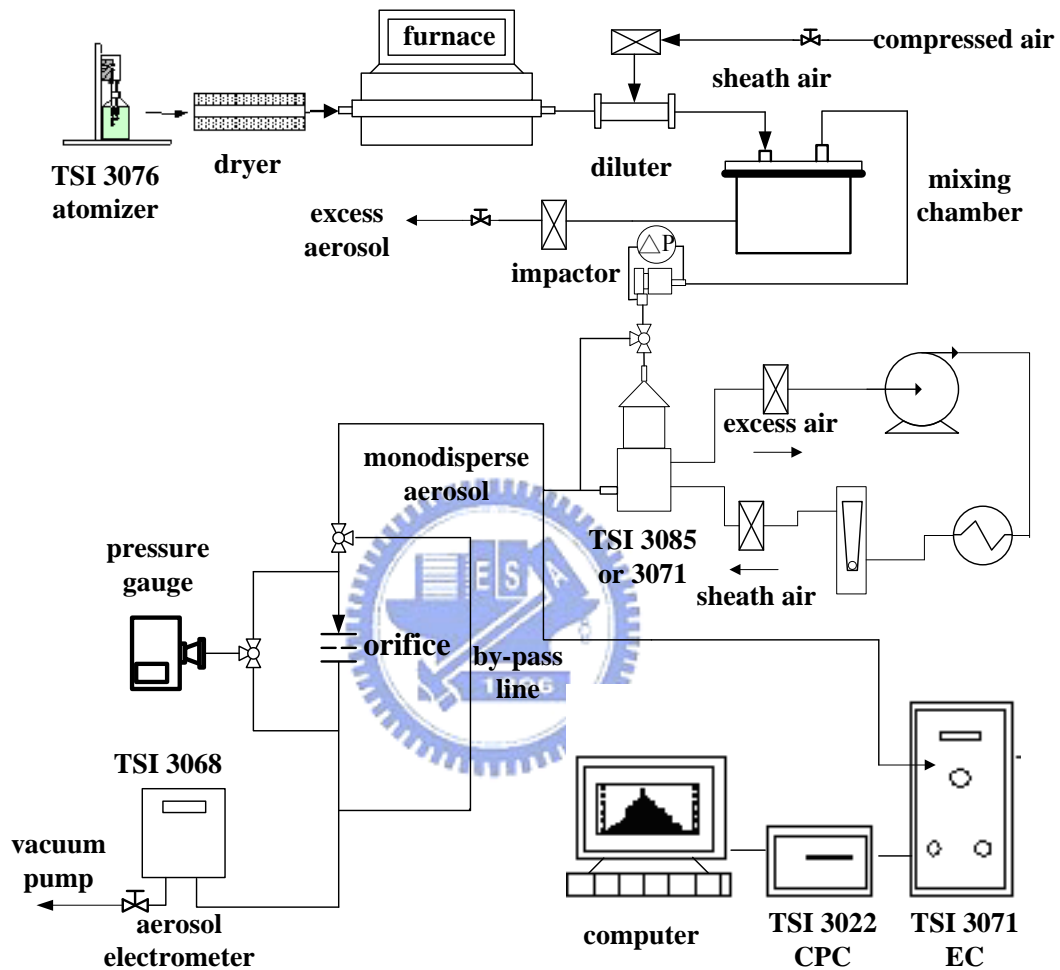


Figure 3.1 Experimental setup for measuring loss of small particle ($<1 \mu\text{m}$).

For measuring the deposition loss of larger particles ($>1\mu\text{m}$), monodisperse fluorescein OA (oleic acid) particles of size 2-12 μm in aerodynamic diameter were generated by a VOMAG (TSI Model 3450). The experimental setup is shown in Fig. 3.2. The generated particle was introduced into the mixing chamber and the test chamber, in which the orifice assembly was located. The orifice assembly was oriented vertically upward in the test chamber with the inlet tube at the top. The air velocity in the test chamber was nearly zero. The electrostatic neutralizer (Kr-85) was used with the TSI VOMAG to neutralize particles and the APS (TSI Model 3321) was used to monitor the size and uniformity of the particles. A pressure gauge (Varian Model CT-100) was used to monitor the pressure at the upstream and downstream of the orifice.

After introducing monodisperse fluorescein OA particles into the orifice assembly for about 30 minutes, fluorescein OA particle loss in each part of the orifice assembly was determined in the similar way as the NaCl particles, except that the cotton swabs were dissolved in xylene after wiping fluorescein OA particles and the solution were analyzed by a fluorometer (Turner Designs Model 10-AU-005). The deposition efficiency at IT, OP, OB and TAO was also calculated by the same way as in Eq. (3.2).

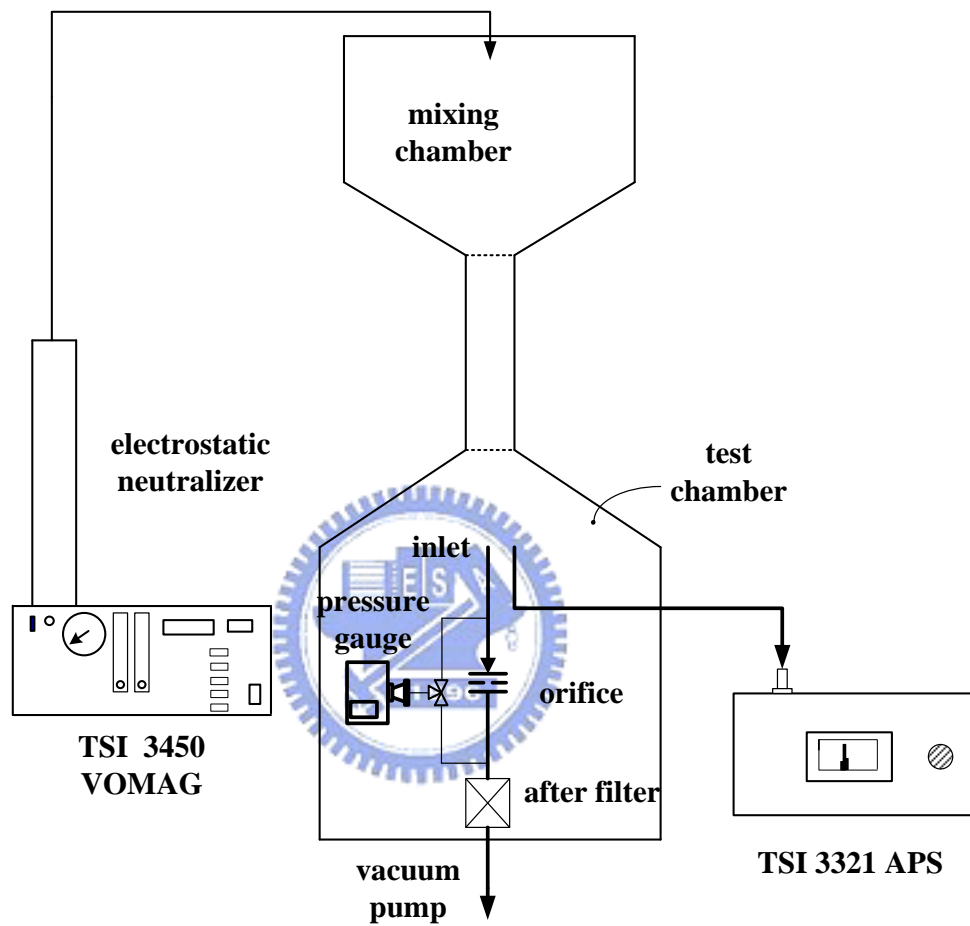


Figure 3.2 Experimental setup for measuring loss of larger particle (2-15 μm).

3.1.2 Particle collection efficiency of the axial flow cyclone

The experimental system for collection efficiency test of the axial flow cyclone is shown in Fig. 3.3. Monodisperse OA ($\rho_p = 894 \text{ kg/m}^3$) and NaCl ($\rho_p = 2200 \text{ kg/m}^3$) particles in diameter between 12 and 100 nm were generated also by the atomization and electrostatic classification technique. Polydisperse particles were first generated by atomizing (Atomizer, TSI Model 3076) 0.05 or 0.1% (v/v) OA and NaCl solution. Then the aerosol flow was dried by a silica gel drier. The dried aerosol stream was passed through a furnace (Lindberg/Blue Model CC58114C-1) and mixed with clean air to produce sufficiently small particles ($< 100 \text{ nm}$) after the furnace. The temperature of the furnace was fixed at 350 and 880 °C for OA and NaCl particles, respectively. Fine polydisperse particles were generated by mixing the vapor with dry compressed air. Monodisperse, singly charged particles were generated by classifying the polydisperse particles by a nano-DMA (TSI Model 3085).

The SMPS (Condensation Particle Counter, TSI Model 3022 and Electrostatic Classifier, TSI Model 3071) was used to monitor the concentrations of particles in the monodisperse particle stream from the nano-DMA. The concentrations were used to correct for the multiple charge effect on the collection efficiency.

An aerosol electrometer (TSI Model 3068) was used to measure the electric current of the upstream and downstream aerosol concentrations of the cyclone. A homemade Faraday cage with a larger inlet and outlet than the TSI Model 3068 electrometer was used to reduce the pressure drop through it.

A critical orifice (O'Keefe Controls Co., E-8, 0.351 slpm or E-9, 0.455 slpm or E-10, 0.566 slpm) was installed at the cyclone inlet to achieve the low-pressure condition. A powerful vacuum pump (DUO 65, Pfeifeer, Germany, nominal pumping speed: $70 \text{ m}^3/\text{hr}$) was used to achieve the desired low pressure conditions. The inlet pressures at the cyclone inlet in this study are 4.3, 6.0 5.4, 6.8 and 7 Torr.

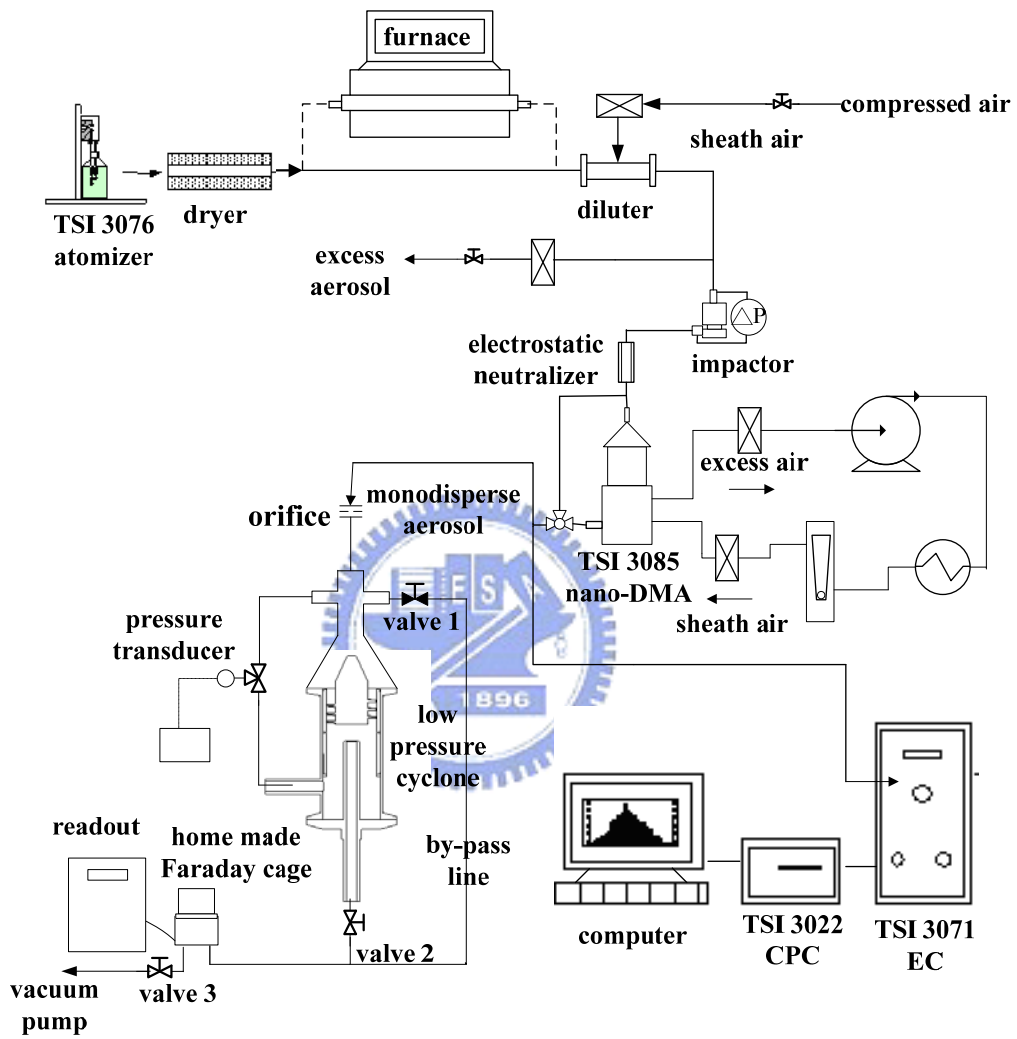
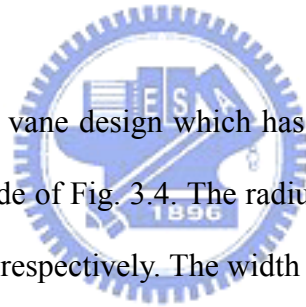


Figure 3.3 Experimental setup for testing collection efficiency of the cyclone.

The bypass line was used to determine the particle concentration at the cyclone inlet which can be controlled by an on-off valve (valve 1) as shown in Fig. 3.3. When valve 1 is open and valve 2 is closed, the aerosol flow will pass through the bypass line and the inlet aerosol concentration can be measured. On the other hand, when valve 1 is closed and valve 2 is open, the aerosol flow will pass through the cyclone and the particle concentration at the cyclone outlet can be obtained. By adjusting the angle valve (valve 3) at the downstream of the Faraday cage, the pressure at the cyclone inlet can be controlled.

The loading effect test was conducted by introducing polydisperse particles continuously into the cyclone of vane over a period of time. The particle collection efficiency was tested after loading polydisperse particles (total number conc.: $8.26 \times 10^6 \sim 1.29 \times 10^7$ #/cm³, NMD: 69.5~82 nm, σ_g : 1.53~1.58) for 1-h (loaded mass: 0.33 mg), 3-h (1.24 mg), and 5-h (1.73 mg), respectively.

Schematic diagram of the vane design which has one vane and makes 3 complete turns was shown in the right-hand side of Fig. 3.4. The radius of the spindle and the inner radius of the cyclone are 10 and 15 mm, respectively. The width and the height of the vane section are 5 and 4 mm, respectively. The left-hand side of Fig. 3.4 shows the detailed geometries of the spindle and vane.



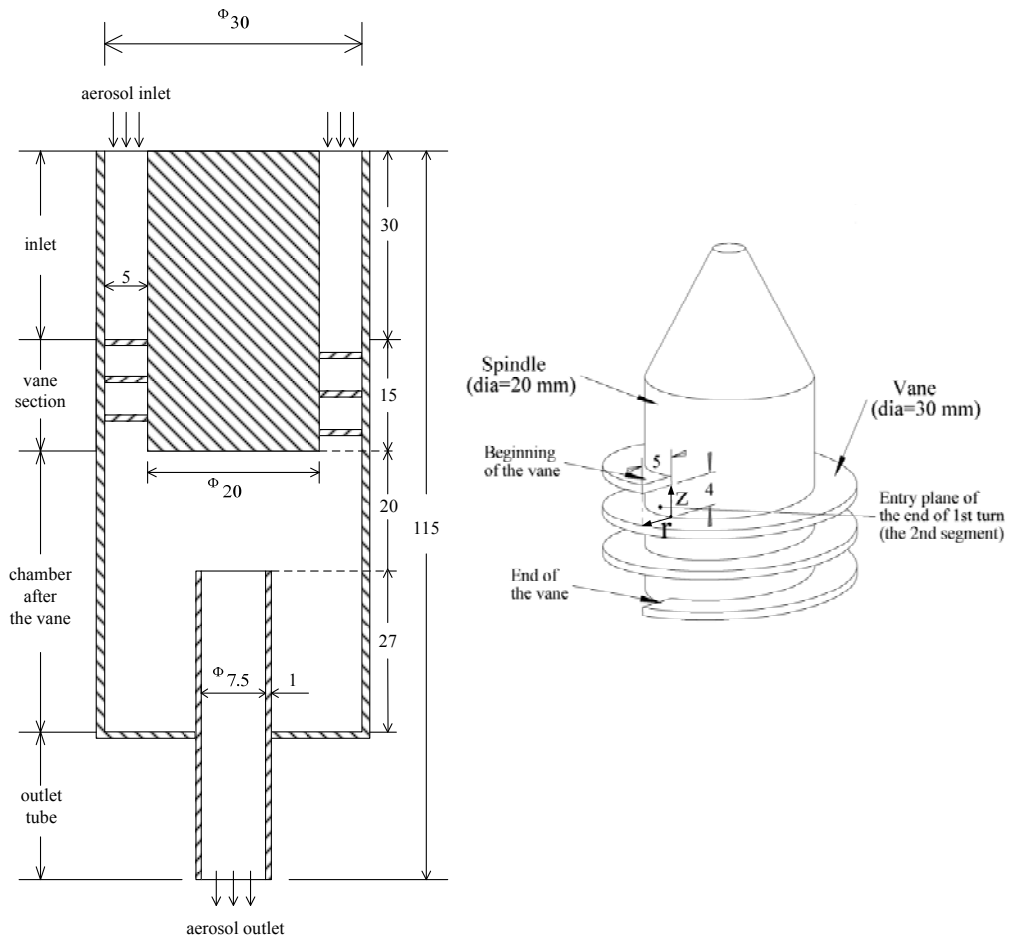


Figure 3.4 Schematic diagrams of the spindle and vane design. (the r-z coordinate and the dimension of the vane section are also indicated.)

3.2 Theoretical method for particle collection efficiency of the axial flow cyclone

In this study, a theoretical equation for calculating particle collection efficiency of the cyclone was derived. According to the equation and the numerical results of flow field, the numerical results of particle collection efficiency and an empirical equation for predicting the cutoff aerodynamic diameter of the cyclone were obtained.

As a particle enters the cyclone, it experiences the centrifugal force and migrates toward the wall. The Stokes law was adopted to calculate the particle drag force since the Re_p (particle Reynolds number) was much smaller than 0.1 of the cyclone. The particle radial velocity and hence the collection efficiency is calculated theoretically based on the gas volumetric flow rate, properties of the cyclone, carrying gas and particles. The transit time of a particle in the vane section, t_v , is given by the ratio of the effective volume in the vane section (Vol) to the gas volumetric flow rate (Q). The effective volume in the vane, Vol , is


$$Vol = \pi (r_{\max}^2 - r_{\min}^2) n (P - Nw) \quad (3.3)$$

Therefore the particle (or gas) transit time in the vane section, t_v , is

$$t_v = \frac{\pi (r_{\max}^2 - r_{\min}^2) n (P - Nw)}{Q} \quad (3.4)$$

The average tangential gas velocity in the vane section, \bar{V}_t , can be calculated as

$$\bar{V}_t = \frac{2 \pi r_{\min} n N}{t_v} = \frac{2 r_{\min} Q N^2}{(r_{\max}^2 - r_{\min}^2) (P - Nw)} \quad (3.5)$$

Due to centrifugal force $\bar{V}_t^2 \tau / r$, the particle will move in the radial direction. Neglecting the transient state of particle motion, the steady state particle radial velocity, V_r , is

$$V_r = \frac{dr}{dt} = \frac{\tau \bar{V}_t^2}{r} = \frac{4\tau r_{\min}^2 Q^2 N^2}{r(r_{\max}^2 - r_{\min}^2)^2 (P - Nw)^2} \quad (3.6)$$

where τ is the particle relaxation time, which is written as

$$\tau = \frac{\rho_{p0} D_{pa}^2 C_c(D_{pa})}{18\mu} \quad (3.7)$$

where $C_c(D_{pa})$ is the slip correction factor of D_{pa} particle.

Based on Eq. (3.6), the differential radial migration distance of particle, dr , can be calculated as

$$dr = V_r dt = \frac{\tau \bar{V}_t^2}{r} \frac{rd\theta}{\bar{V}_t} = \tau \bar{V}_t d\theta \quad (3.8)$$

Integrating Eq. (3.8), the total particle radial migration distance Δr can be calculated. Then the collection efficiency, η_a of the particle can be calculated as

$$\eta = \frac{\Delta r}{r_{\max} - r_{\min}} \quad (3.9)$$

3.3 Numerical method

3.3.1 Flow field of the critical orifice assembly

In order to obtain the flow field in the orifice, a 3-D numerical simulation was conducted in the present study. The governing equations are Navier-Stokes and the continuity equations. Since the gas velocity inside the orifice in this study is supersonic, steady-state and compressible laminar flow ($Re \ll 2000$) was assumed in the simulations. The Navier-Stokes and the continuity equations were solved by using the STAR-CD 3.22 code (CD-adapco Japan Co., LTD) which is based on the finite volume discretization method. The pressure-velocity linkage was solved by the PISO algorithm (Issa, 1986) and the UD (upwind differencing) and CD (central differencing) schemes were used for the space discretization methods of the flow velocity and density, respectively. Hexahedral cells which allow for finer grids near the wall were generated by an automatic mesh generation tool, Pro-Modeler 2003 (CD-adapco Japan Co., LTD). The total numbers of cells used were 500,000 and 1,000,000. The average cell length was around 0.25 or 0.2 mm and the smallest length of 0.005 mm was assigned near the wall.

The convergence criterion of the flow field calculation was set to be 0.1 % for the summation of the residuals. The total number of iterations was about 500 and the time required to reach convergence was about 3000 minutes. Non-slip condition was applied on the walls and the constant mass flow rate (0.455 slpm) was set on the inlet boundary assuming uniform velocity profile. On the outlet boundary, a fixed pressure was assigned based on the experimental data.

3.3.2 Particle loss in the critical orifice assembly

The flow field of the orifice was calculated first. For calculating diffusional loss of nanoparticles (<100 nm), the concentration field of nanoparticles was calculated based on the following convection-diffusion equation:

$$\frac{\partial \rho}{\partial x_j} \left(u_j m_s - D_s \frac{\partial m_s}{\partial x_j} \right) = 0 \quad (3.10)$$

where subscript s denotes the species, m_s and D_s are the mass fraction (kg/kg) and the diffusivity (m^2/s) of the species, respectively. After the concentration field was obtained, particle loss (kg/s) due to diffusion was then calculated at the surfaces of different parts of the orifice assembly as

$$J_y = -D_s \left. \frac{\partial C}{\partial y} \right|_{y=0}, \quad (3.11)$$

$$\text{total loss} = \iint J_y d_x d_z. \quad (3.12)$$



In the above equations, J_y , D_s and C are mass flux in y direction (kg/s m^2), diffusivity of nanoparticles (m^2/s) and mass concentration of nanoparticles (kg/m^3), respectively. Once the total loss of the nanoparticles was obtained, deposition efficiency was then calculated as a ratio of the total loss to the incoming mass flow rate of nanoparticles.


For calculating inertial impaction loss of large particles, particle trajectories were calculated after the flow field was obtained. In order to track the particle location in the computational domain, the computational cells had to be tetrahedral instead of hexahedral used in the calculation of diffusion loss of nanoparticles. The equation of particle motion was solved numerically by using the fourth order Runge-Kutta integration to obtain the particle trajectories. In the Cartesian coordinate, the particle equations of motion in x , y and z directions are:

$$m \frac{dV_x}{dt} = C_D \text{Re}_p \frac{C_c}{24\tau} (U_x - V_x) \quad (3.13)$$

$$m \frac{dV_y}{dt} = C_D \text{Re}_p \frac{C_c}{24\tau} (U_y - V_y) \quad (3.14)$$

$$m \frac{dV_z}{dt} = C_D \text{Re}_p \frac{C_c}{24\tau} (U_z - V_z) - mg. \quad (3.15)$$

In the above equations, subscript x , y and z denote the velocity in x , y and z directions, respectively; V and U are the velocities of the particle and flow (m/s); Re_p and C_D are the particle Reynolds number and the empirical drag coefficient; m is particle mass (kg); g is the gravitational acceleration (m/s^2). C_D was expressed by Rader and Marple (1985) as a function of Re_p :

$$C_D = \begin{cases} \frac{24}{\text{Re}_p}, & \text{for } \text{Re}_p \leq 1 \\ \frac{24}{\text{Re}_p} (1 + 0.0916 \text{Re}_p), & \text{for } 1 < \text{Re}_p \leq 5 \\ \frac{24}{\text{Re}_p} (1 + 0.158 \text{Re}_p^{2/3}), & \text{for } 5 < \text{Re}_p \leq 1000 \end{cases} \quad (3.16)$$


where Re_p is defined as

$$\text{Re}_p = \frac{\rho(U - V)D_p}{\mu} \quad (3.17)$$

where ρ is the density of air (kg/m^3). In this study, a dilute suspension of particles in a perfect gas was assumed. Particle-particle interactions were neglected and the presence of particles was assumed not to affect the gas flow.

Particles were released at the inlet tube entrance and the trajectories of the particles were

calculated by integrating Eqs. (3.13)-(3.15). In the calculation, the method of Schafer and Breuer (2002) was used to determine which tetrahedral cell a particle was located. If the vertices of a regular tetrahedral are designated by P1, P2, P3 and P4 as shown in Fig. 3.5, the difference vectors $\overrightarrow{P1P2}$, $\overrightarrow{P1P3}$ and $\overrightarrow{P1P4}$ are linearly independent and form a three-dimensional space for the cell. Any particle position P* (x^* , y^* , z^*) in space can be written as

$$\begin{cases} \alpha(x_4 - x_1) + \beta(x_2 - x_1) + \gamma(x_3 - x_1) = x^* - x_1 \\ \alpha(y_4 - y_1) + \beta(y_2 - y_1) + \gamma(y_3 - y_1) = y^* - y_1 \\ \alpha(z_4 - z_1) + \beta(z_2 - z_1) + \gamma(z_3 - z_1) = z^* - z_1 \end{cases} \quad (3.18)$$

where α , β and γ are fractions of the difference vectors $\overrightarrow{P1P4}$, $\overrightarrow{P1P2}$ and $\overrightarrow{P1P3}$, respectively and can be calculated analytically. If point P* is located inside a tetrahedral cell (such as point P5 shown in Fig. 3.5), α , β and γ should meet the following criteria (Schafer and Breuer, 2002):

$$\begin{cases} \alpha \geq 0 \\ \beta \geq 0 \\ \gamma \geq 0 \\ \alpha + \beta + \gamma \leq 1 \end{cases} \quad (3.19)$$

If one or more of these conditions are violated, the particle is not in the cell. Then the computer program proceeds to the adjacent cells until the cell containing the particle is found. The adjacent cells are the cells which have more than one joint vertices with the particle's original cell. The list of the adjacent cells will be updated when the particle moves to another cell. The program will stop when the particle touches the wall or leaves the computational domain.

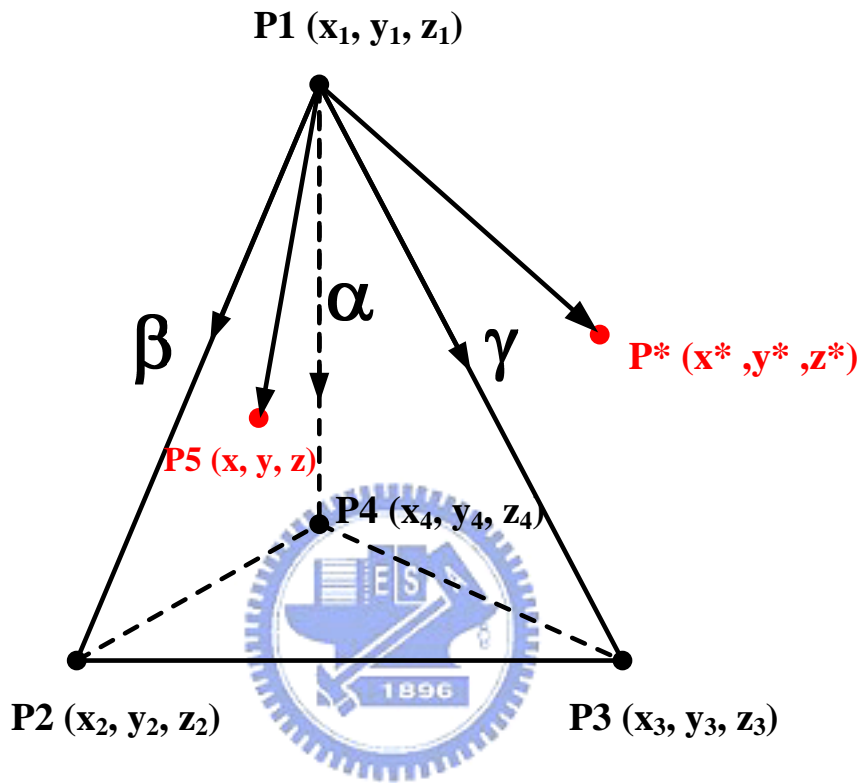


Figure 3.5 Schematic diagram of a tetrahedral cell.

In the calculation of particle trajectory, time step, Δt , for each iteration was calculated based on the cell size and particle velocity as

$$\Delta t = \frac{0.1L_{\min}}{U_{\max}} \quad (3.20)$$

where L_{\min} and U_{\max} are the minimum length and maximum flow velocity, respectively, of the cells adjacent to the particle's present cell.

The critical particle trajectory method was used to obtain the impaction deposition efficiency of the particle at different parts of the orifice. In the simulation, particles were found to deposit only in the collection regions OP (the front surface of the orifice plate) and TAO (the tube after the orifice), no particles deposited in OB (the back side of the orifice). The critical particle radial positions and collection regions of particles at OP and TAO are shown in Fig. 3.6. If a particle starts at a radial position greater than r_{OP} and smaller than r_0 at the entry plane, it will deposit at the collection region OP which is the annular area from r_{OP} to r_0 shown in the figure. If the particle starts at a radial position smaller than r_{OP} and greater than r_{TAO} , it will deposit at the collection region TAO which is the annular area from r_{TAO} to r_{OP} shown in the figure. Otherwise, the particle will not deposit in the orifice.

The deposition efficiencies of the particle at OP, η_{OP} , and TAO, η_{TAO} , were respectively calculated as

$$\eta_{OP} = \frac{r_0^2 - r_{OP}^2}{r_0^2} \quad \text{and} \quad \eta_{TAO} = \frac{r_{OP}^2 - r_{TAO}^2}{r_0^2}. \quad (3.21)$$

After obtaining η_{OP} and η_{TAO} , the penetration of the particle was then calculated as $1 - \eta_{OP} - \eta_{TAO}$.

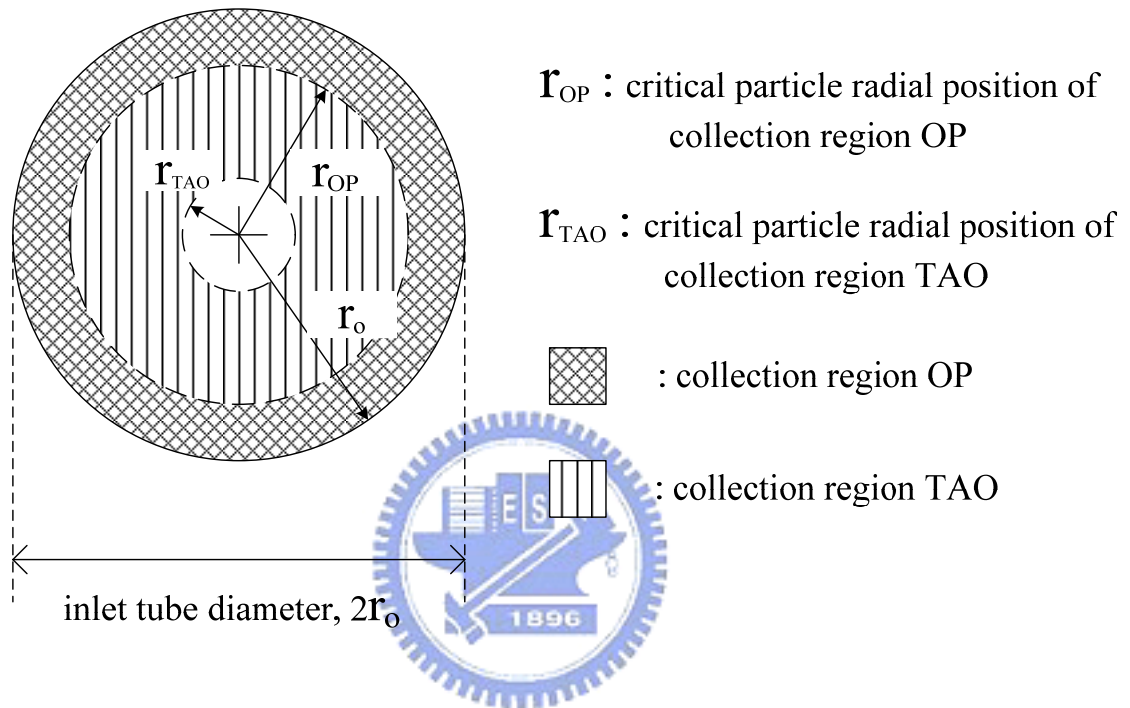


Figure 3.6 Critical particle radial positions and collection regions at the entry plane of the inlet tube. (OP: orifice plate; TAO: tube after orifice)

3.3.3 Particle collection efficiency of the axial flow cyclone

In order to obtain accurate flow and pressure fields of the axial flow cyclone, 3-D numerical simulation was conducted. The computational domain is shown in Fig. 3.4. Since the maximum Knudsen number in the cyclone corresponding to outlet pressure, P_{out} , of 1.46 Torr (inlet pressure $P_{in}=4.31$ Torr) is around 0.01 in the present study, the flow was considered as a continuum. The maximum Knudsen number, $K_{n,max}$ is defined as

$$K_{n,max} = \frac{2\lambda}{D_{out}}, \quad (3.22)$$

where D_{out} is the inner diameter of the outlet tube of the cyclone (m); λ is the mean free path of the air molecules (m). The methods for calculating the flow field were the same as section 3.3.1 expect the computational cell types and the pressure-velocity linkage algorithm were different. The type chosen was the hybrid cells which contained both hexahedral and tetrahedral types. The hybrid cells allow for finer grids close to the wall and match the vane geometry. The pressure-velocity linkage here was solved by the SIMPLE algorithm (semi-implicit method for pressure linked equation) (Pantankar, 1980).

The paraboloid flow was assumed to calculate the particle migration distance. Since the flow in the cyclone was found to spin for slightly greater than 2 turns starting slightly ahead of the end of the first turn and ending slightly beyond the end of the third turn, only the particle migration distance during 2 turns was calculated. To simplify the calculation, the total radial migration distance of a particle, Δr , was calculated based on Eq. (3.8) as the sum of the migration distance from ten segments of the vane section, each segment corresponded to 1/4 turn of the vane. The first segment or the first 1/4 turn was added before the end of the first turn while another 1/4 turn was added after the end of the third turn. The second and third turn each constituted four segments in the calculation. All together there were 10 segments. As will

be shown later, the tangential flow develops very fast and becomes nearly fully developed near the end of the first turn of the vane. The fully developed profile is paraboloid which can be written as

$$V_{t,n^{th}}(r, z) = 2(\bar{V}_{t,n^{th}} - 1) \left[1 - \left(\frac{2z}{4} \right)^2 \right] \left[1 - \left(\frac{2r}{5} \right)^2 \right] + 2, \quad (3.23)$$

where the coordinates r and z are illustrated in Fig. 3.4 shown later. $V_{t,n^{th}}(r, z)$ and $\bar{V}_{t,n^{th}}$ are the tangential velocity of the entry plane of the n^{th} segment at position (r, z) and the average tangential velocity of the n^{th} segment, respectively. The constant 2 m/s at the right-hand side of Eq. (3.23) represents the tangential velocity near the wall, which is obtained from the numerical simulation shown later. If the total migration distance of a particle of aerodynamic diameter, D_{pa} , and the initial radial position is greater than 5 mm (or $r_{\max} - r_{\min}$, the width of the vane section) then the particle hits the wall and is collected. Assuming different initial radial positions of a particle at the entry plane of the first segment, the critical curve which delineates the collection and non-collection regions of the particle can be found. As the collection area is obtained, then the collection efficiency of D_{pa} particles can be calculated by the following equation as

$$\eta_{D_{pa}} = \frac{Ac \times \bar{V}'_{t,1}}{5 \times 4 \times \bar{V}_{t,1}}, \quad (3.24)$$

where Ac is the collection area (mm^2); $\bar{V}'_{t,1}$ is the average tangential velocity of the collection area (m/s); 5 mm and 4 mm are the width and gap of the vane section, respectively (mm); $\bar{V}_{t,1}$ is the average tangential velocity at the entry plane of the 1st segment of the vane section.

Since the pressure drop of the cyclone occurs mainly in the vane section, $\bar{V}_{t,n^{th}}$ is calculated based on the pressure at the n^{th} section following the ideal gas law and mass conservation principle. For comparison purpose, if the tangential flow field is assumed to be plug flow, the total radial migration distance Δr can be calculated as (referring to Eq. (3.8))

$$\Delta r = \sum_{n^{th}=1}^{10} \frac{\pi}{2} \bar{\tau}_{n^{th}} \bar{V}_{t,n^{th}}, \quad (3.25)$$

where $\bar{V}_{t,n^{th}}$ is the average tangential velocity (m/s), $\bar{\tau}_{n^{th}}$ is the average relaxation time of the particle. Both $\bar{V}_{t,n^{th}}$ and $\bar{\tau}_{n^{th}}$ depend on the average pressure at the n^{th} segment.

3.3.4 Brownian Dynamic simulation of particle collection efficiency

For simulating the cyclone collection efficiency, the Lagrangian method was used for calculating particle trajectories. For each particle diameters, particle trajectories of 10,000 particles uniformly distributed in the inlet were calculated. When a particle touched the wall of the cyclone it was assumed to have been collected by the cyclone. Neither bounce-back nor re-suspension of previously deposited particles was taken into account. The collection efficiency was calculated as the number of particles deposited in the cyclone divided by the number of particles entering the cyclone, or 10,000. This number was chosen to obtain reliable results in a reasonable computational time.

For small particles, the stochastic momentum exchange with bombarding gas molecules becomes significant. BD simulation was used to include the influence of diffusional motion on particle deposition. The equation of the particle motion can be written as the following Langevin equation (Kanaoka et al., 1983):

$$m \frac{dV}{dt} = F^{(D)} + F^{(ext)} + F^{(B)}, \quad (3.26)$$

where m is the particle mass, V is the particle velocity, $F^{(D)}$ is the drag force on the particle, $F^{(ext)}$ denotes the external force and $F^{(B)}$ is the rapidly fluctuating, random force resulting from the particle bombardment by gas molecules. Thus $F^{(B)}$ can be defined as

$$F^{(B)} = mA(t). \quad (3.27)$$

where $A(t)$ is the random acceleration of the particle (m/s^2). In this study, no other external force but the gravitational force was considered. But the gravity was found to be negligible as compared to the drag force. The drag force is given by

$$F^{(D)} = \frac{3\pi\mu D_p}{C_c} (U - V), \quad (3.28)$$



The BD simulation was established by Chandrasekhar (1943) for Stokesian particles in a stationary fluid ($U=0$) and force free field ($F^{(ext)}=0$). The Chandrasekhar's first lemma was:

$$M = \int_0^t \psi(\xi) F^{(B)}(\xi) / m d\xi. \quad (3.29)$$

The function $\psi(\xi)$ was defined to be

$$\psi(\xi) = \tau \left(1 - \left[\exp\left(-\frac{\xi-t}{\tau}\right) \right] \right), \quad (3.30)$$

Then the probability distribution of M is given by

$$\varphi(M) = \frac{\exp[-|M|^2 / 4q \int_0^t \psi^2(\xi) d\xi]}{\left[4\pi q \int_0^t \psi^2(\xi) d\xi \right]^{3/2}}, \quad (3.31)$$

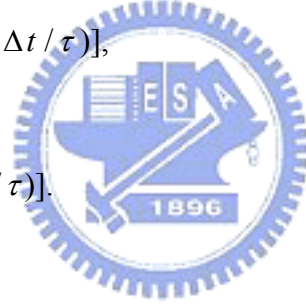
where q is defined as

$$q = \frac{k_B T}{\tau m}. \quad (3.32)$$

From Eq. (3.31), expected values of particle displacement in the i -th direction $\langle \Delta L_i \rangle$ and its velocity change $\langle \Delta V_i \rangle$ during time interval Δt can be found as

$$\langle \Delta L_i \rangle = V_i \tau [1 - \exp(-\Delta t / \tau)], \quad (3.33)$$

$$\langle \Delta V_i \rangle = V_i [1 - \exp(-\Delta t / \tau)]. \quad (3.34)$$



The standard deviations of displacement σ_{L_i} and particle velocity change σ_{V_i} has been derived to be

$$\sigma_{V_i} = \sqrt{(1 - \exp(-2\Delta t / \tau)) k_B T / m}, \quad (3.35)$$

$$\sigma_{L_i} = \sqrt{(2\Delta t / \tau - 3 + 4 \exp(-\Delta t / \tau) - \exp(-2\Delta t / \tau)) k_B T / (m / \tau^2)}. \quad (3.36)$$

In this study, extension of BD in the case of moving fluid with external forces derived by Podgórski (2002) was used. Integration of Langevin equation for a time interval small enough that the host fluid velocity U and external forces $F^{(ext)}$ may be assumed constant over $(t, t + \Delta t)$,

gives the following bivariate normal density probability distribution function, $\varphi_i(\Delta V_i, \Delta L_i)$

$$\varphi_i(\Delta V_i, \Delta L_i) = \frac{1}{2\pi\sigma_{V_i}\sigma_{L_i}\sqrt{1-\rho_c}} \exp\left\{-\frac{1}{2(1-\rho_c^2)}\left[\left(\frac{\Delta V_i - \langle\Delta V_i\rangle}{\sigma_{V_i}}\right)^2 - \frac{2\rho_c(\Delta V_i - \langle\Delta V_i\rangle)(\Delta L_i - \langle\Delta L_i\rangle)}{\sigma_{V_i}\sigma_{L_i}} + \left(\frac{\Delta L_i - \langle\Delta L_i\rangle}{\sigma_{L_i}}\right)^2\right]\right\}. \quad (3.37)$$

where ρ_c is the coefficient of correlation.

The distribution may be rearranged to a more convenient form as the product of two Gaussian distributions:

$$\varphi_i(\Delta V_i, \Delta L_i) = \left\{ \frac{1}{\sqrt{2\pi}\sigma_i} \exp\left[-\frac{1}{2}\left(\frac{\Delta V_i - \langle\Delta V_i\rangle}{\sigma_{V_i}}\right)^2\right] \right\} \times \left\{ \frac{1}{\sqrt{2\pi(1-\rho_c^2)}\sigma_{L_i}} \exp\left[-\frac{1}{2}\left(\frac{\Delta L_i - \langle\Delta L_i\rangle - \rho_c\sigma_{L_i}(\Delta V_i - \langle\Delta V_i\rangle)/\sigma_{V_i}}{\sigma_{L_i}\sqrt{1-\rho_c^2}}\right)^2\right] \right\}. \quad (3.38)$$

The expected values of particle velocity change $\langle\Delta V_i\rangle$ and the linear displacement $\langle\Delta L_i\rangle$ are then equal to

$$\langle\Delta V_i\rangle = [U_i - V_i + F_i^{(ext)} / (m / \tau)] [1 - \exp(-\Delta t / \tau)], \quad (3.39)$$

$$\langle\Delta L_i\rangle = [U_i + F_i^{ext} / (m / \tau)] \Delta t - [1 - \exp(-\Delta t / \tau)] [U_i - V_i + F_i^{ext} / (m / \tau)] \tau, \quad (3.40)$$

while standard deviations, σ_{V_i} , σ_{L_i} , are calculated by Eq. (3.35) and (3.36), respectively. The coefficient of correlation, ρ_c , is defined as

$$\rho_c = [1 - \exp(-\Delta t / \tau)]^2 \{ [1 - \exp(-2\Delta t / \tau)] [2\Delta t / \tau - 3 + 4 \exp(-\Delta t / \tau) - \exp(-2\Delta t / \tau)] \}^{1/2} \quad (3.41)$$

We can therefore formulate the following generalized algorithm for the BD simulation. For a given initial particle position and its initial velocity components, V_i , at a moment t , the fluid velocity, u_i , and the external forces, $F_i^{(ext)}$ then can be calculated. Then, one calculates expected values $\langle \Delta V_i \rangle$, $\langle \Delta L_i \rangle$ from Eqs. (3.39-3.40), the standard deviations σ_{V_i} , σ_{L_i} , from Eqs. (3.35-3.36), and the correlation coefficient, ρ_c from Eq. (3.41). Next we generate two independent random numbers, G_{L_i} , G_{V_i} , having Gaussian distribution with zero mean and unit variance. Finally, we calculate the change of the particle velocity, ΔV_i , and the particle linear displacement, ΔL_i , during the time-step Δt from the expression accounting for deterministic and stochastic motion as

$$\Delta V_i = \langle \Delta V_i \rangle + G_{V_i} \sigma_{V_i}, \quad (3.42)$$

$$\Delta L_i = \langle \Delta L_i \rangle + \rho_c G_{V_i} \sigma_{L_i} + (1 - \rho_c^2) G_{L_i} \sigma_{L_i}. \quad (3.43)$$

All the above steps are repeated for each coordinate, $i=1,2,3$. Having determined the increments ΔV_i and ΔL_i , the new particle velocity at the moment $V_i(t+\Delta t) = V_i + \Delta V_i$ and in the same manner the new particle position is calculated. After completing one-time step of simulations, the next step is performed in the same way. The time step was calculated as the minimum side-length of each cell divided by the flow velocity at the cell center. Decreasing the time step was shown not to affect the simulated collection efficiency. The computation of the particle trajectory stops when the particle touches the wall or exits the computation

domain. After calculating the trajectories of all 10,000 particles at the inlet, the collection efficiency of the particle can be determined.



CHAPTER 4

RESULTS AND DISCUSSION

4.1 Particle loss in the critical orifice assembly

4.1.1 Diffusion loss

The comparison of diffusional deposition efficiencies between the present experimental data and simulated results is shown in Fig. 4.1. It shows that diffusion loss increases with decreasing flow rate and particle diameter because smaller particles have larger diffusivity and lower flow rate leads to longer particle residence time. The experimental data are in very good agreement with the simulated results with the maximum deviation of less than 5%. Diffusion loss is not severe when downstream pressure, P_{od} , is 260 Torr (critical condition, 0.455 slpm). Diffusion loss is zero when the particle is greater than 40 nm and it increases from 0 to 3.5% as particle is decreased to 15 nm. In contrast, diffusion loss is more severe as P_{od} is increased to 602 Torr (non-critical condition, 0.242 slpm). The loss is increased from about 0 to 25% as particle is decreased from 100 to 15 nm. From the simulation, diffusion loss is found to increase sharply as particle is decreased below 15 nm but experimental data are not available. The loss is about 25 and 45% for P_{od} of 260 and 602 Torr, respectively when particle is 5 nm.

Diffusion loss at different parts of the orifice assembly was also calculated. When $P_{ou}=260$ Torr and $D_p=15$ nm, the loss in the IT, OP, OB and TAO is 2.3, 0.26, 0.32 and 5.3%, respectively, in which most of the loss occurs at TAO. There is a high radial flow velocity of about 15 m/s moving toward the wall at about 15-20 mm downstream of the orifice, which creates a recirculation region behind the orifice. This could contribute to a significant deposition of nanoparticles at TAO.

4.1.2 Inertial impaction loss on the front surface of the orifice

Fig. 4.2 shows the comparison of the present experimental data with simulated deposition efficiencies on front surface of the orifice (OP), and previous numerical results of Sato et al. (2002), Ye and Pui (1990) and Muyschondt et al. (1996). The present data are in agreement with the present simulated results and the model of Muyschondt et al. (1996), while very large deviation exists for the models of Ye and Pui (1990) and Sato et al. (2002). As an example, when $St_o(I-A_o/A_i)=0.1$, the models of Ye and Pui (1990) and Sato et al. (2002) predict the loss to be 0%, while the model of Muyschondt et al. (1996) predicts 10% loss, compared to the measured loss of approximately 6.3% and the present simulated loss of 8.4%.

Present simulation overestimates deposition efficiency slightly with a maximum deviation of 3.5% from the data. The model of Muyschondt et al. (1996) predicts the deposition efficiency slightly better than the present simulation for $St_o(I-A_o/A_i)<0.06$ (corresponding to 1.4 μm particle of this study at $P_{od}=260$ Torr), while the present simulation outperforms that of Muyschondt et al. (1996) for $St_o(I-A_o/A_i)>0.06$. In addition, the simulated results are close to the models of Ye and Pui (1990) and Sato et al. (2002) at $St_o(I-A_o/A_i) >0.4$ (corresponding to 13 μm particle of this study).

In Fig. 8 of Ye and Pui (1990), the numerical model is seen to agree with the experimental data for $St_o(I-A_o/A_i)$ larger than 0.3. However, deviation occurs in the region when $St_o(I-A_o/A_i) <0.3$. Similar to the present data, their experimental data show that deposition efficiency has a long tail at small particle size. Ye and Pui (1990) claimed that the deviation was probably due to diffusion and interception depositions neglected in their model. However, the present simulation does show a long tail even when diffusion is neglected. Muyschondt et al. (1996) found their turbulent model improved the accuracy of inertial impaction efficiency for small $St_o(I-A_o/A_i)$ when compared to the laminar model of Ye and Pui (1990). In the present simulation, laminar flow was assumed yet good agreement was

obtained for small $St_o(I-A_o/A_i)$.

In order to reduce particle deposition loss on the surface of the orifice, Chen and Pui (1995) proposed to modify the inlet tube with a conical contraction. They found that the deposition efficiency would decrease efficiently with decreasing contraction angles for a fixed $St_o(I-A_o/A_i)$. For example, at a fixed $St_o(I-A_o/A_i)$ of 0.5 (corresponding to 15 μm particle of present study), the deposition efficiencies are 35, 30, 20, 10 and 5% for contraction angles of 90, 60, 45, 30 and 15°, respectively. Modifying the present orifice plate to have a contraction half-angle below 30° is expected to reduce the inertial impaction loss below 5% for particle as large as 15 μm in aerodynamic diameter.



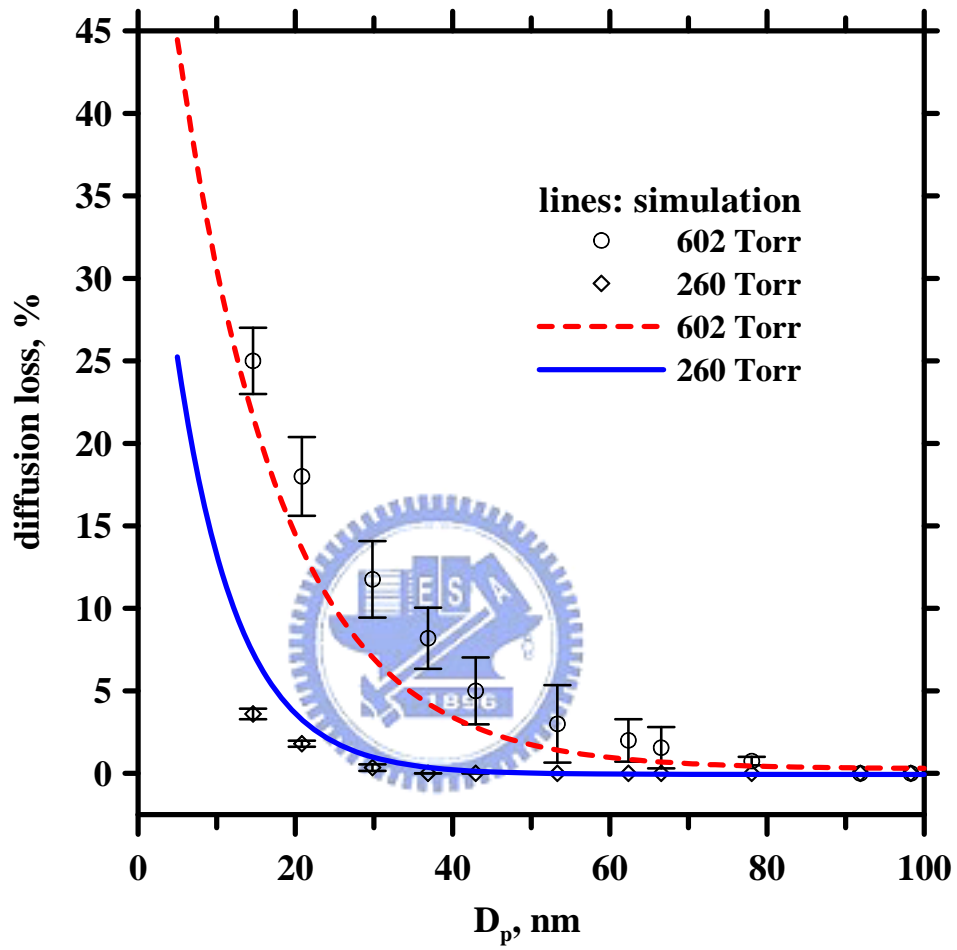


Figure 4.1 Comparison of simulated diffusional deposition efficiencies with experimental data.

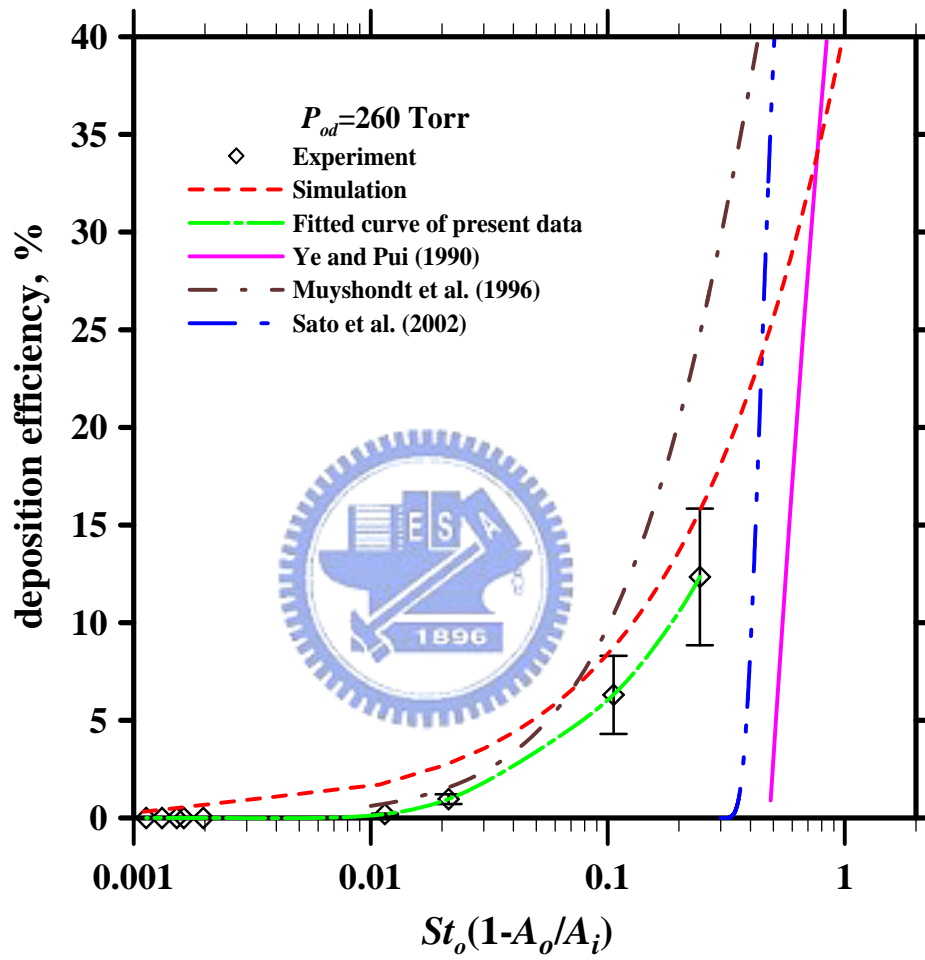


Figure 4.2 Particle deposition efficiency on the front surface of the orifice.

4.1.3 Inertial impaction loss in the downstream tube of the orifice

Fig. 4.3 shows the comparison of the particle deposition efficiency on the tube wall after the orifice (TAO) between the present experimental data, simulated results and the previous results of Pui et al. (1998). The simulated results are seen in very good agreement with the experimental data with a maximum difference of about 10%. The present data and simulated results are in agreement with the results of Pui et al. (1998) when the $SQRT(St')$ is less than 1

while the disagreement exist as $SQRT(St') > 1$. Note $SQRT(St') = \sqrt{\frac{St_o U_o}{U_i}} (D_o / D_i)^{0.58}$ as in Eq.

(2.10). Both present experimental and simulated results of deposition efficiency peak near $SQRT(St')=1$ (or 2.1 μm in aerodynamic diameter D_{pa} of this study), while the deposition efficiency is reduced with increasing $SQRT(St')$ as $SQRT(St') > 1$. In contrast, the fitted curve of Pui et al. (1998) increases with increasing $SQRT(St')$ even when $SQRT(St') > 1$. The reason why this discrepancy happens is because the data of Pui et al. (1988) are limited for $SQRT(St')$ smaller than 1. Nonetheless, both results of Pui et al. (1998) and present study can be used to predict particle loss in the TAO for $SQRT(St')$ between 0.1 to 1. For $SQRT(St')$ larger than 1, the present results must be used.

The peak deposition efficiencies of the present data and simulated results are 83 and 78.3%, respectively, corresponding to 2.8 μm particles in aerodynamic diameter. The experimental deposition efficiency is reduced to about 49% at $SQRT(St')=4.4$ (or $D_{pa}=10 \mu\text{m}$). As explained earlier in section 4.1.1, there is a high radial flow velocity of about 15 m/s moving toward the wall at the downstream of the orifice due to jet expansion. This expanding flow results in large particle inertial impaction loss on the tube wall after the orifice for $SQRT(St')$ between 0.6 to 2 (or D_{pa} from 1.5 to 5 μm). However, for particles with $SQRT(St') > 2$ (or $D_{pa} > 5 \mu\text{m}$), they do not follow the expanding jet flow as readily as smaller particles. Therefore, their inertial impaction loss at TAO is smaller. Small particles with $SQRT(St') < 0.6$

stay close to the centre axis of the orifice during jet expansion resulting in small impaction loss at TAO and high penetration efficiency (Liu et al., 1995; Lee et al., 2003). To reduce particle loss at TAO, Lee et al. (1993) suggested to design a big expansion chamber instead a small outlet tube after the orifice, which is able to reduce $SQRT(St')$ and impaction loss.

From the current results, peak particle deposition in the TAO can be reduced to less than 40% if $SQRT(St')$ is reduced below 0.5 which corresponds to the outlet tube diameter of 25 mm. This was verified by another simulation in which all geometries were kept the same except the outlet tube diameter was increased from 6.2 to 25 mm. Table 4.1 summarizes the comparison of $SQRT(St')$ and particle loss in the TAO for outlet tube diameters of 6.2 and 25 mm. The maximum loss of the 2.8 μm particle is reduced from 78.3% to 38.3% and the loss of other particle sizes is also reduced by more than 50%.

4.1.4 Particle loss at different parts of the orifice

Both experimental and simulated deposition efficiencies at different parts of the orifice assembly for different size particles are shown in Fig. 4.4. It is seen the loss is not severe at IT and OB, while significant loss is found in OP and TAO. At OP, the experimental and simulated particle losses both increase with increasing particle size (or St_o). At $P_{od} = 260$ Torr, the experimental particle loss is 0.2, 0.97, 6.31 and 12.35% for particles of 2, 2.8, 6.5 and 10 μm in aerodynamic diameter. The simulated results show good agreement with the data with a maximum deviation within 4.5 %.

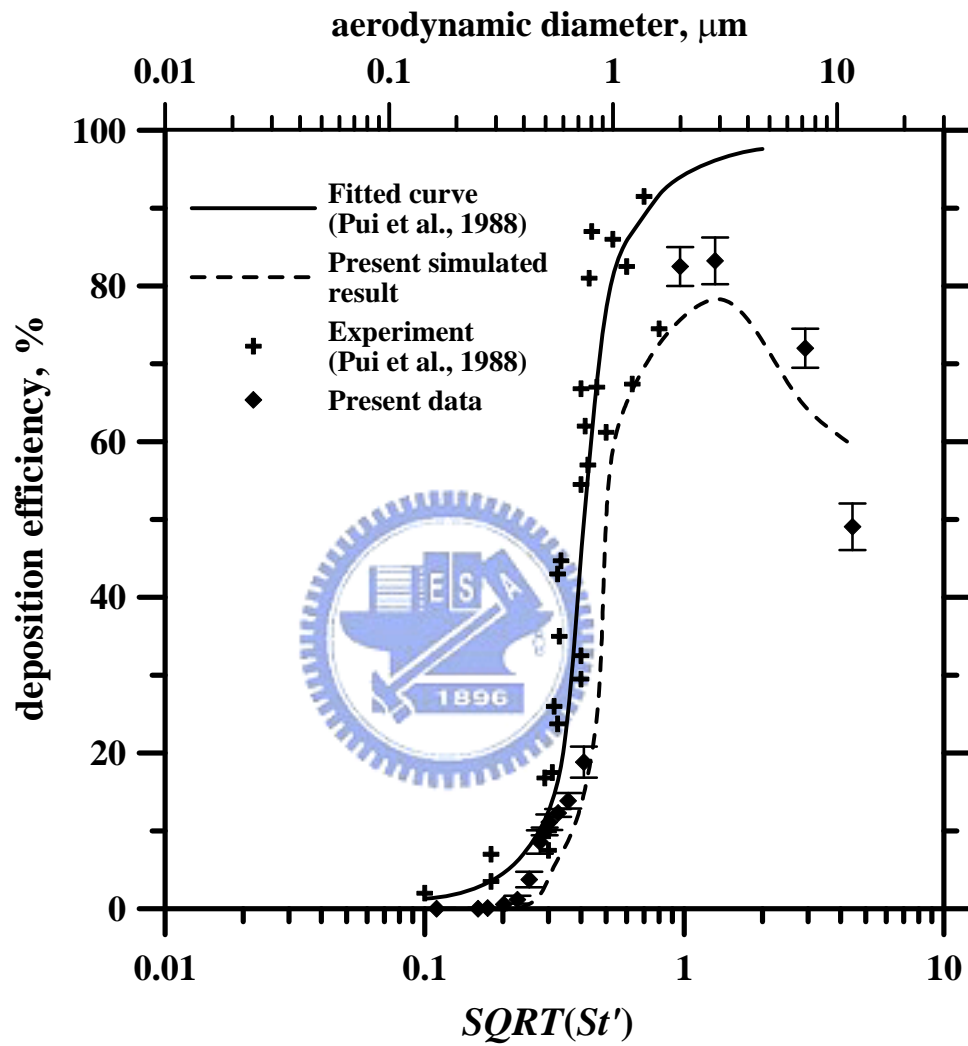


Figure 4.3 Particle deposition efficiency on the tube after the orifice.

Table 4.1 Comparison of $SQRT(St')$ and particle loss in the TAO for different outlet tube diameters, $P_{od}=260$ Torr.

$P_{od}=260$ Torr	D_{pa} (μm)	2	2.8	6.5	10
6.2 mm	loss (%)	75.7	78.3	64.5	59.5
	$SQRT(St')$	0.96	1.31	2.92	4.45
25 mm	loss (%)	25.0	38.3	33.0	21.1
	$SQRT(St')$	0.37	0.50	1.11	1.68



The experimental particle deposition efficiency at TAO is 82.5, 83.2, 72.0% for particle sizes of 2, 2.8, 6.5 and 10 μm , respectively, in aerodynamic diameter. The simulated results are also in good agreement with the data with a maximum deviation within 10.5 %.

In the present collection efficiency experiment of the axial flow cyclone, the flow after the orifice was in critical condition and the tested particles were all larger than 10 nm. From Fig. 4.1, the diffusion loss of nanoparticles in the upstream of the cyclone is found to be negligible.

In the present low pressure cyclonic separator, the maximum value of $SQRT(St')$ is nearly 0.57 for $P_{in}= 5.4$ Torr at 0.455 slpm, $P_{in}= 6.77$ Torr at 0.566 slpm and $P_{in}= 4.31$ Torr at 0.351 slpm for 100 nm particles. From Fig. 4.3, the corresponding loss is about 50 %. Although this particle loss did not affect the experimental accuracy since the upstream particle concentration of the cyclone was equal to that in the downstream of the orifice, it is desirable to reduce nanoparticle loss in other applications such as particle classification and sampling. If the inner diameter of the outlet tube is increased from 6.2 to 25 mm, the loss of 100 nm particles is reduced from 50 to 0%, as shown in Table 4.2.

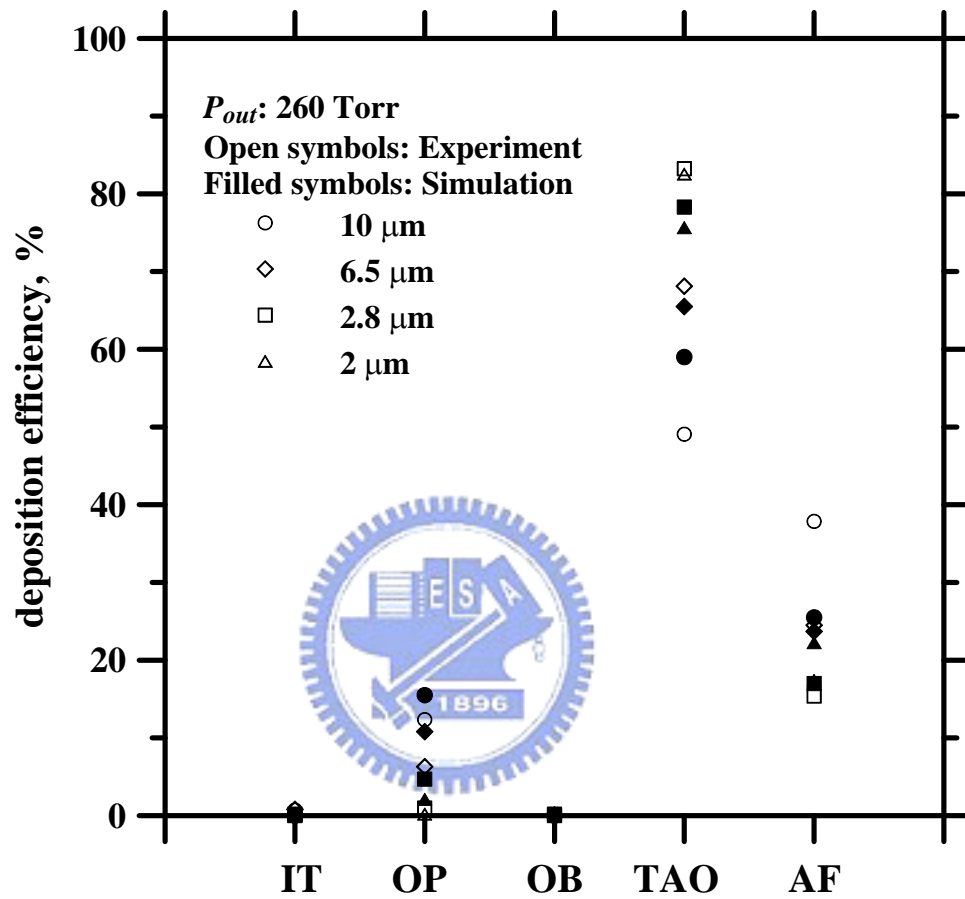


Figure 4.4 Particle deposition efficiency on different parts of the orifice assembly.

Table 4.2 Comparison of $SQRT(St')$ and particle loss in the TAO for different outlet tube diameters, $P_{od}=5.4$ Torr.

$P_{od}=5.4$ Torr	D_{pa} (nm)	50	100
6.2 mm	loss (%)	15	50
	$SQRT(St')$	0.4	0.57
25 mm	loss (%)	0	0
	$SQRT(St')$	0.18	0.26



4.2 Particle collection efficiency of the axial flow cyclone

4.2.1 Comparison of liquid and solid particles

The collection efficiencies of solid NaCl and liquid OA particles for the inlet pressure of 6 and 5.4 Torr and the sampling flow rate of 0.455 slpm are compared in Fig. 4.5. For OA particles, the present experimental data are in good agreement with our previous data (Tsai et al., 2004). The collection efficiencies are seen to be greatly improved for both OA and NaCl particles when the pressures at the cyclone inlet are reduced from 6 to 5.4 Torr. The cutoff aerodynamic diameters of OA and NaCl particles are reduced from 49.8 and 47.1 to 23.1 and 21.2 nm, respectively as the pressure at the cyclone inlet is decreased from 6 to 5.4 Torr, respectively. In addition, Fig. 4.5 indicates that the collection efficiencies of liquid and solid particles are close to each other for both operation pressures except in the size range from 60 to 120 nm at 6 Torr where the collection efficiency of OA is slightly better (within 10%) than NaCl. This is to say that the effect of solid particle bounce on the collection efficiency is insignificant. Furthermore, it also found the diffusion effect on collection efficiency for particles less than (40 nm) is not as significant as claimed by Hsu et al. (2005).

4.2.2 Solid particle loading effect

The effect of polydisperse particle loading on the collection efficiency is shown in Fig. 4.6 for the inlet pressure of 6 and 5.4 Torr, respectively. For both operating pressures, the collection efficiency after 1-h loading (loaded mass: 0.33 mg) is 5-10 % higher than that of a clean cyclone (or zero particle loading). However, the collection efficiency after 3-h (1.24 mg), and 5-h (1.73 mg) loading is not too much different from that of 1-h loading. Tsai et al. (1999) used two monodisperse particles, 3.76 and 6.7 μm in aerodynamic diameter, to examine the solid loading effect on the collection efficiency of a 10 mm nylon cyclone. Both loaded particle masses in the cyclone were 0.06 mg. Their experimental results indicated that

the particle penetration decreased (or collection efficiency increased) for both loading conditions compared to that of the clean condition. The present results also show that the collection efficiency increases after particles are loaded in the cyclone. However, the increase in the collection efficiency is larger in Tsai et al. (1999) (10-30 % increases, small 10 mm tangential flow cyclone) than the present study (5-10 % increases, axial flow cyclone). This is due to the accumulation of deposited particles on the cyclone wall opposite to the inlet for the small tangential flow cyclone, which has a larger influence on the collection efficiency. In comparison, the present axial flow cyclone has a larger cyclone diameter and a more uniform particle deposit on the cyclone wall. As a result, the solid particle loading effect on the collection efficiency is not as significant as that of the small tangential flow cyclone.



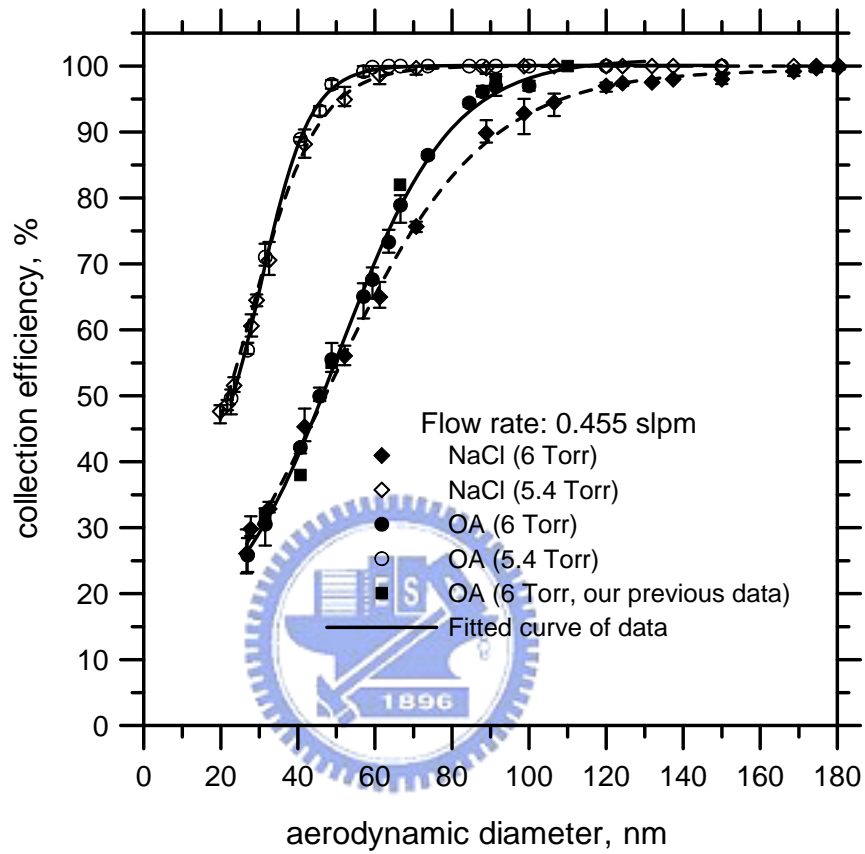


Figure 4.5 Particle collection efficiency versus aerodynamic diameter for solid NaCl and liquid OA particles at different inlet pressures.

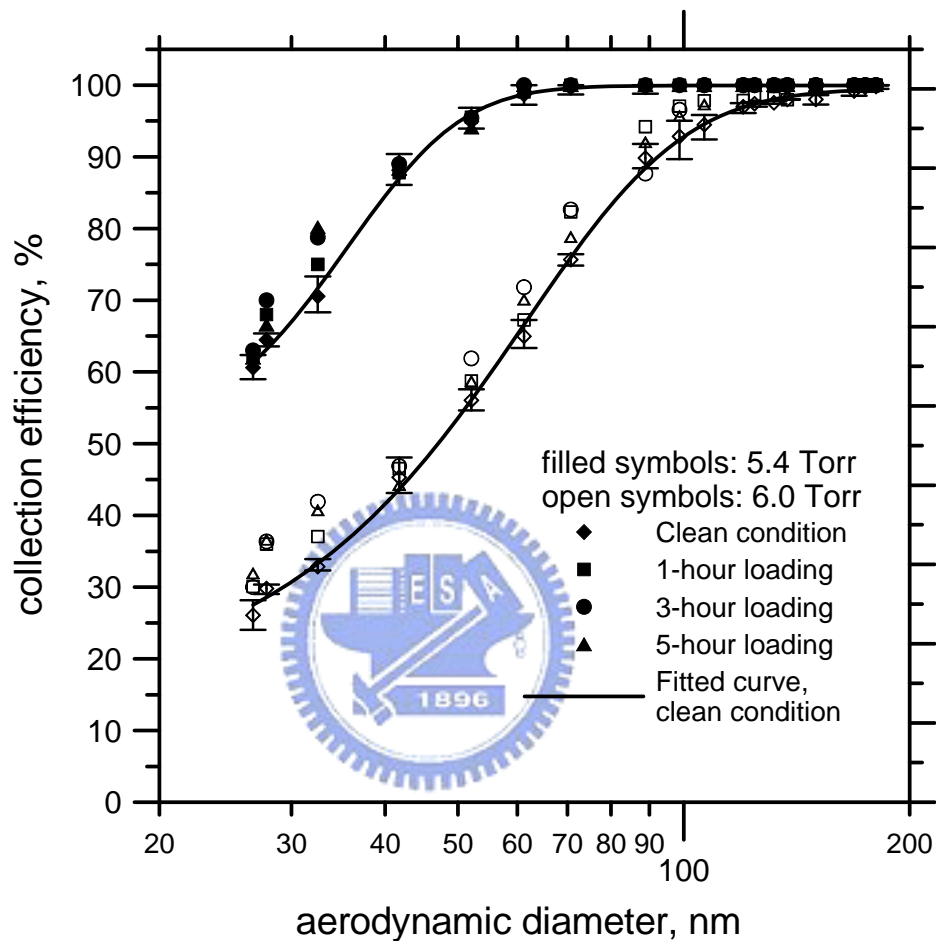


Figure 4.6 Particle loading effect on collection efficiency, solid NaCl particles.

4.2.3 Collection efficiency of OA particles at different operating conditions

The collection efficiency of liquid OA particles at 5 different inlet pressures is shown in Fig. 4.7. The flow rate and the Reynolds number range from 0.351 to 0.566 slpm and 4.9 to 8.0, respectively. The Reynolds number, Re , is defined as

$$Re = \frac{\rho(r_{\max} - r_{\min})\bar{V}_a}{\mu}, \quad (4.1)$$

where \bar{V}_a is the average axial velocity (m/s). ρ , \bar{V}_a , and μ were evaluated at the entry of the vane section. The figure shows that the parameter A , which is defined as $A = P_{in} \times P_{out} / Q_o$ (P_{in} : pressure at the cyclone inlet; P_{out} : pressure at the vane outlet), influences the collection efficiency and cutoff diameter. The larger A is the smaller collection efficiency the cyclone becomes. The cutoff size is 21.7, 23.1, 25.6 nm for the inlet pressure of 4.3 Torr at 0.351 slpm ($A=17.93$), 5.4 Torr at 0.455 slpm ($A=22.08$), and 6.8 Torr at 0.566 slpm ($A=26.19$) (also shown in Table 1). The cutoff size becomes much larger for the inlet pressure of 7.0 Torr at 0.566 slpm ($A=36.73$), 6.0 Torr at 0.455 slpm ($A=43.12$) as the parameter A becomes much larger for these two cases (also shown in Table 1). The reasons why the cutoff size is affected by A will be explained later when the empirical equation for cutoff size is derived.

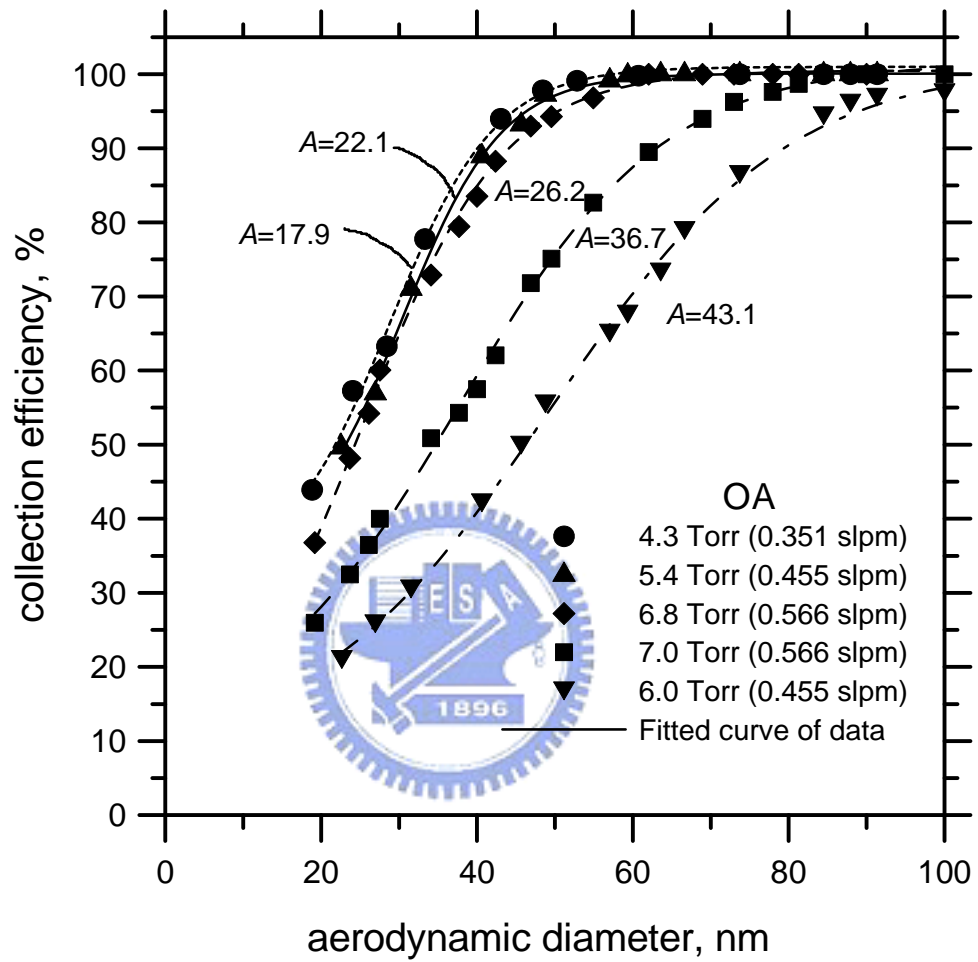


Figure 4.7 Particle collection efficiency versus aerodynamic diameter for OA particles at different inlet pressures and flow rates. (parameter $A=P_{in} \times P_{out}/Q_0$)

4.3 Numerical results for flow field and particle collection efficiency of the cyclone

4.3.1 Simulated flow and pressure fields

The simulated results for the pressure distribution and the maximum tangential velocity in the vane section for $P_{in} = 5.4$ Torr (0.455 slpm) are shown in Fig. 4.8. It can be seen that the tangential velocity remains small in the beginning of the first turn of the vane. However, it increases sharply from the entry plane of the first segment (or the beginning of 3/4 turn). Then it increases exponentially until the end of 3 turns (or the ninth segment) and reduces sharply in the tenth segment. The tangential velocity peaks at 187 m/s at the end of 3 turns and is reduced to 60 m/s sharply at the end of 10th segment.

The pressure distribution shown in Fig. 4.8 corresponds well with the tangential velocity distribution. The flow is accelerated in the tangential direction as the pressure is decreased in the vane. The pressure remains at about 735 Pa (5.5 Torr, within 2 % of the experimental data) in the first turn and then drops monotonically in the second and third turns. Finally, the pressure remains nearly constant at 260 Pa (1.95 Torr) after the end of the third turn. That is, the pressure drop occurs almost entirely in the second and third turns. The figure shows that the flow does not make 3 full turns as the vane does. Rather, it makes slightly more than two turns only. This is one of the main reasons why the differences are large between the experimental cutoff aerodynamic diameters and the previous theoretical values in which the tangential flow was assumed to make three full turns and the tangential velocity was assumed to be plug flow.

Figs. 4.9 (a) and (b) show 2-D view of the tangential velocity profile at the vertical cut planes at the end of 2 and 3 turns, respectively. It also shows 3-D view in (c) of the figure. It is seen the tangential velocity peaks near the center of the plane in both figures and the value is about 2 times the average tangential velocity, which was given in Eq. (3.5).

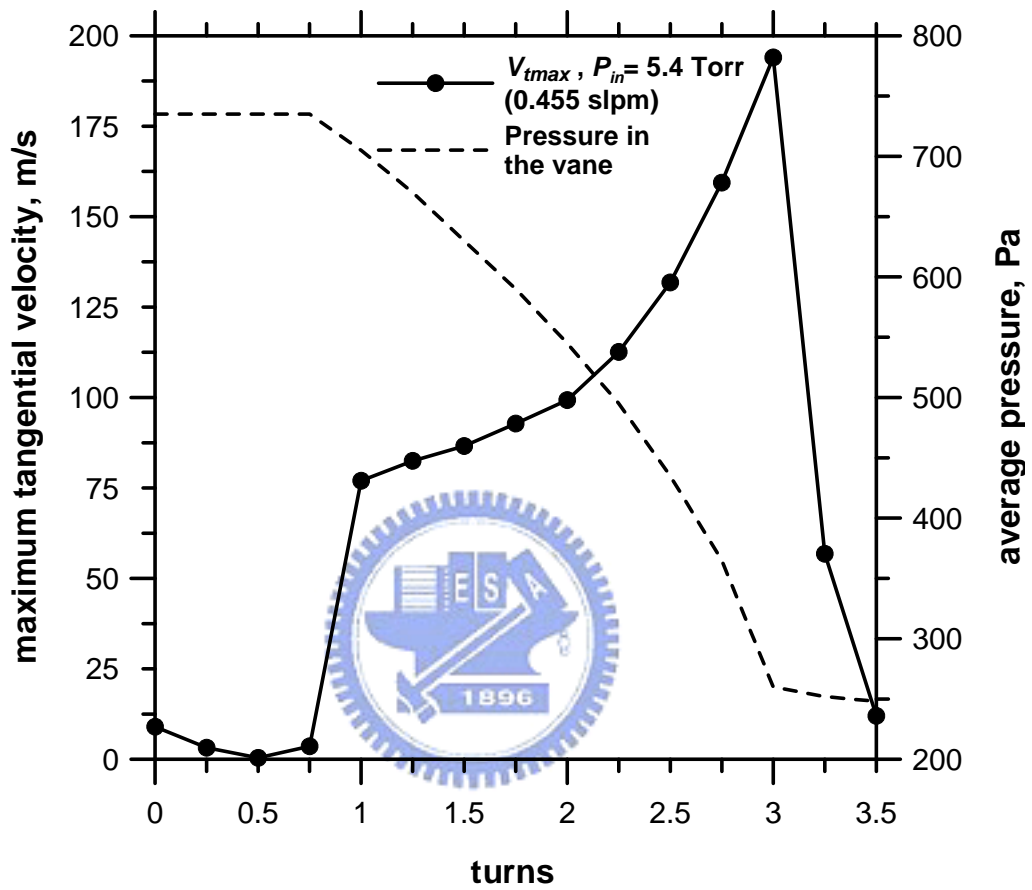


Figure 4.8 Maximum tangential velocity and pressure distribution in the vane, numerical results.

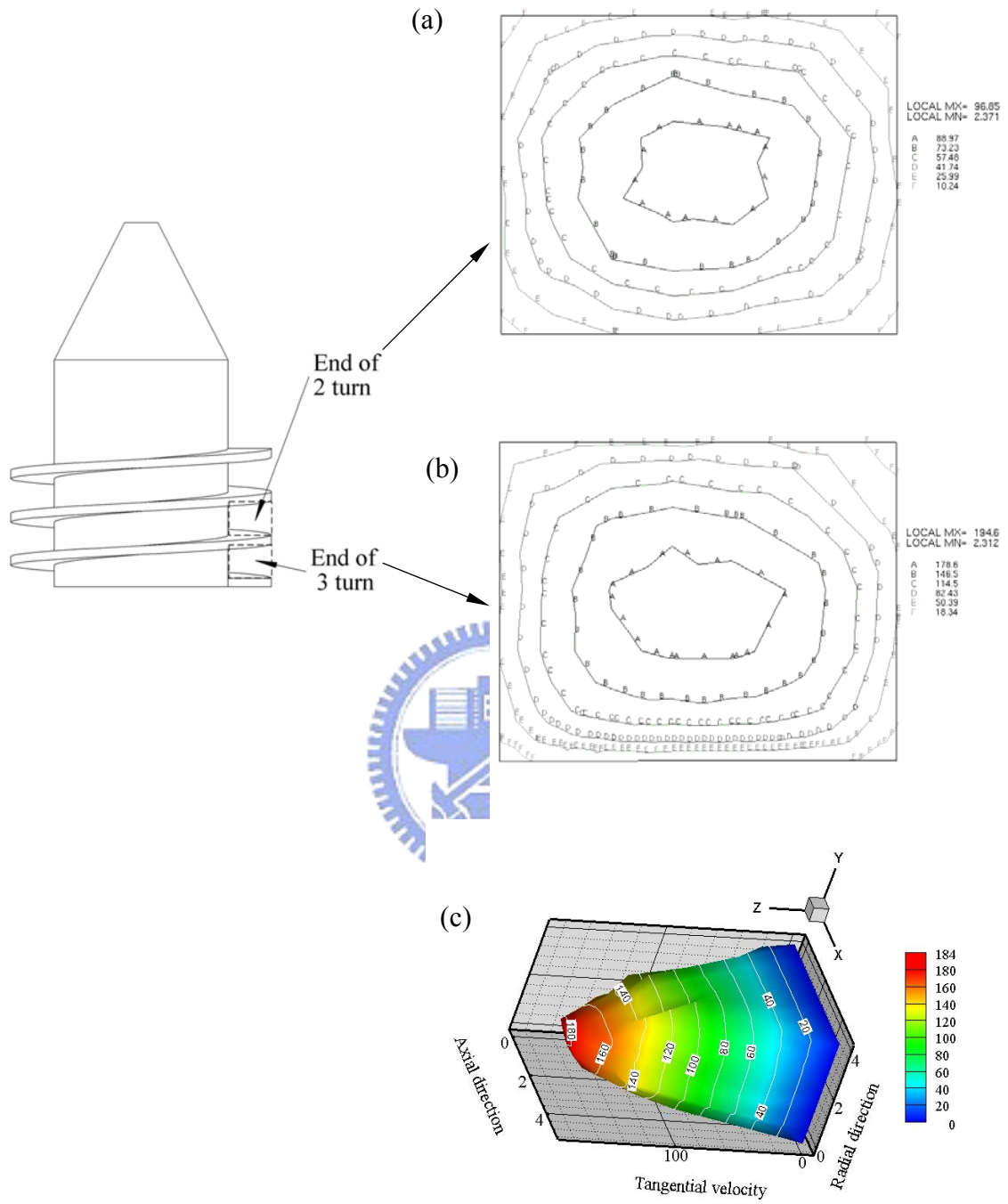


Figure 4.9 Tangential velocity profiles at the cutting plane of the vane section, the end of (a) 2 turns (2-D), (b) 3 turns (2-D) and (c) 3 turns (3-D).

In Eq. (3.5), Q is the volumetric flow rate and can be calculated as

$$Q = Q_0 \frac{P_{760}}{\sqrt{P_{in} P_{out}}} \quad (4.2)$$

It is also found that the velocity near the wall is not zero but about 2 m/s. Similar results can be found in other cut planes and at other different operating conditions ($P_{in} = 4.3, 6, 6.8$ and 7 Torr). From the simulated tangential velocity shown in Figs. 4.9 (a) and (b), the velocity profile is found to be nearly paraboloid, and the variation of velocity with r and z positions can be calculated by Eq. (3.23).

Fig. 4.10 (a) shows the critical collection curves for a 23 nm particle passing through the full 3 turns of the vane with and without considering the tangential velocity of 2 m/s near the wall, respectively. The area to the right hand side of curve is the particle collection region in which a 23 nm particle will be collected in the cyclone when it starts from this region at the entry of the vane section. Otherwise, it won't be collected. By considering the tangential velocity of 2 m/s on the wall was results in an 8 % increase in the collection area, and a similar increase in the collection efficiency. The collection areas of three different particle sizes, 20, 23, and 45 nm, are shown in Fig. 4.10 (b). It shows larger particles have larger collection area than small particles and hence the collection efficiency is also larger.

The experimental particle collection efficiencies and numerical results based on the plug or paraboloid flow assumptions are shown in Fig. 4.11. For the operating conditions at $P_{in} = 4.3, 5.4,$ and 6.8 Torr (Fig. 4.11 (a)), and $P_{in} = 6$ and 7 Torr (Fig. 4.11 (b)). Fig. 4.11 (a) shows that both numerical results agree with the experimental collection efficiencies very well, especially near the cutoff aerodynamic diameter. The error in the numerical prediction of the cutoff aerodynamic diameter by the paraboloid flow assumption is 5.9, 0.7, and 1.5 %, for $P_{in} = 4.3, 5.4,$ and 6.8 Torr, respectively. In comparison, the error by the plug flow assumption

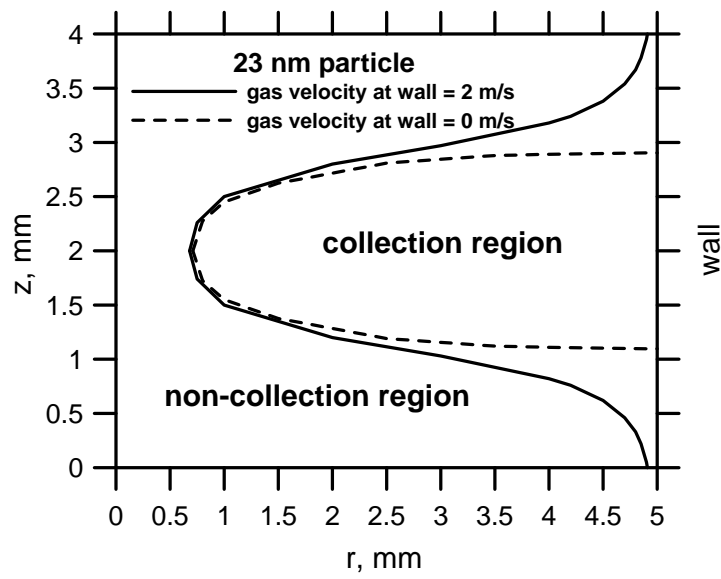
is larger, which is 16.6, 12.8, and 7.7 %, for $P_{in} = 4.3, 5.4,$ and 6.8 Torr, respectively. The plug flow assumption over-estimates while the paraboloid flow assumption under-estimates the collection efficiencies when the particle diameter is greater than the cutoff aerodynamic diameter. The maximum difference for the paraboloid flow assumption is around 12 %, which is slightly better than the plug flow assumption of 15%.

In Fig. 4.11 (b), it is seen larger differences occur between the experimental data and theories than in Fig. 4.11 (a). The error of the cutoff aerodynamic diameter by the paraboloid flow assumptions is 13.9 and 10.1 % for $P_{in} = 6$ and 7 Torr, respectively. In comparison, the error of the plug flow assumption is 25.8 and 11.8 % for $P_{in} = 6$ and 7 Torr, respectively. The paraboloid assumption predicts the cutoff diameter better than the plug flow assumption.

The differences between the numerical results and the experimental data are mainly due to the over-simplified assumption of either plug flow or paraboloid flow. In fact, the flow is developing near the entry of the vane section. Errors may also be caused by the assumption of a constant velocity of 2 m/s near the wall. In addition, calculating the total migration distance Δr from summing the migration distances of ten segments may also induce errors.

Although the present method is good in predicting the cutoff diameter and collection efficiency, it is not possible to obtain an analytical equation to calculate the cutoff diameter. The following section describes a modified empirical method which can be used to predict the cutoff aerodynamic based on the inlet pressure, flow rate, and cyclone dimension.

(a)



(b)

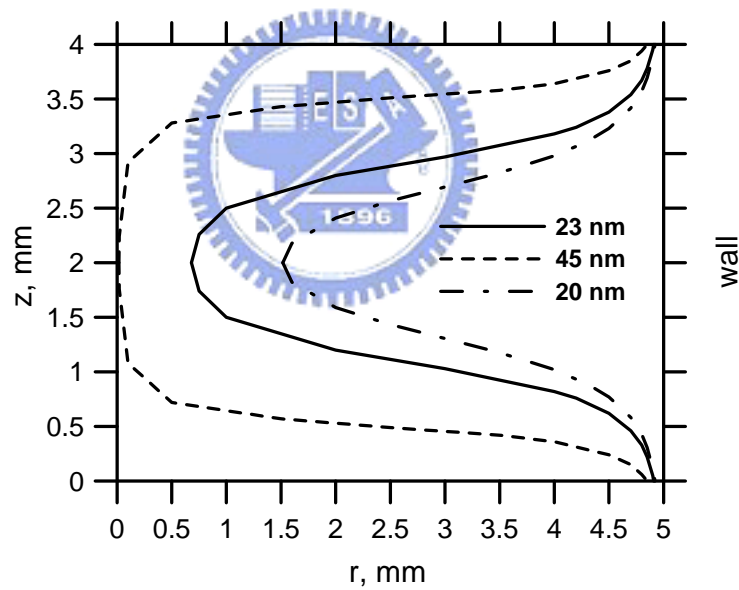
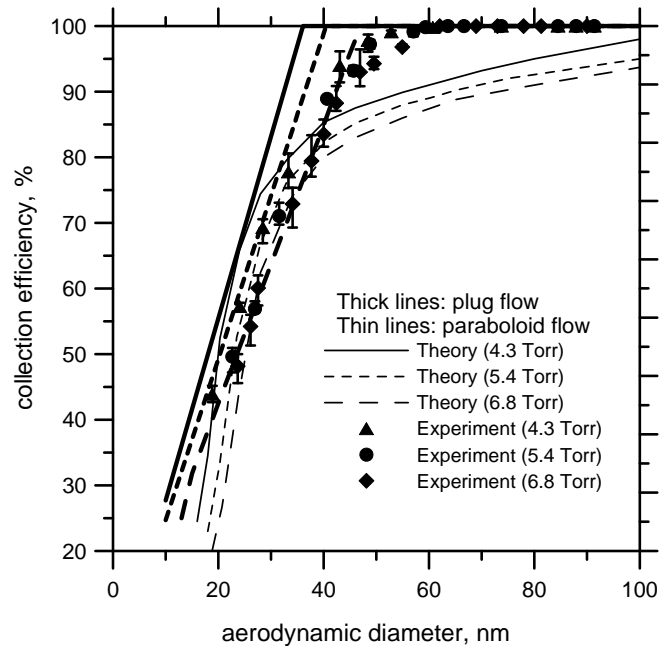


Figure 4.10 Critical curves at the entry plane of the first segment for particle collection. (a) With or without a constant tangential velocity of 2 m/s at the wall for a 23 nm particle. (b) With a constant tangential velocity of 2 m/s at the wall for 20, 23, and 45 nm particles.

(a)



(b)

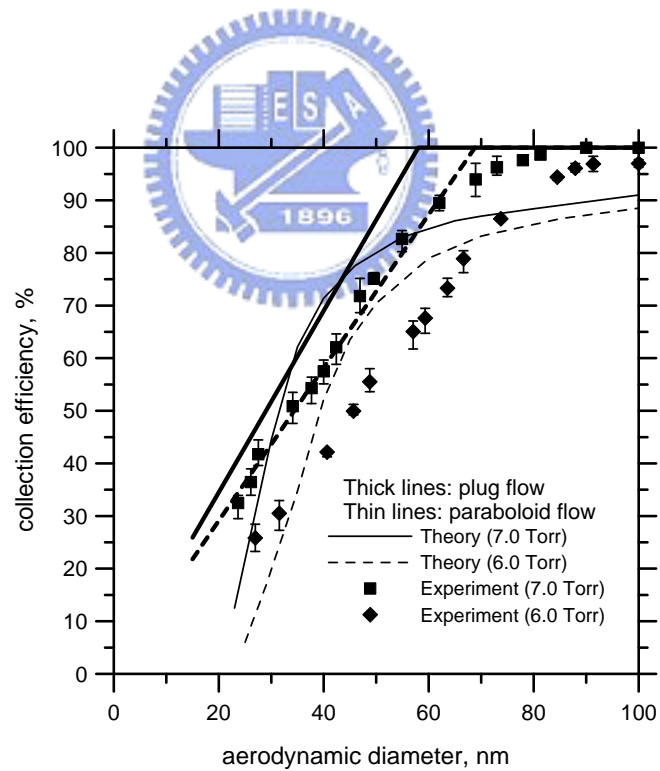


Figure 4.11 Comparison of numerical collection efficiency and experimental data. (a) $P_{in} = 4.3, 5.4, \text{ and } 6.8 \text{ Torr}$. (b) $P_{in} = 6 \text{ and } 7 \text{ Torr}$.

4.3.2 Semi-empirical equation of cutoff aerodynamic diameter

In this study, the theoretical derivation of the particle collection efficiency is similar to our previous study but the pressure drop through the vane section is assumed to be linear. The pressure at n^{th} turn of the vane can be defined based on P_{in} (pressure at the cyclone inlet) and P_{out} (pressure at the vane outlet) as

$$P_n = P_{in} - n \times \frac{P_{in} - P_{out}}{n_T}, \quad (4.3)$$

where the n_T is the total number of turns of the vane and is fixed to 2 based on the present numerical results. The volumetric flow rate and particle relaxation time will change in the vane section with respect to pressure. The plug flow assumption was used to facilitate the derivation of the theoretical collection efficiency, which is known to under-predict the cutoff diameter. By comparing the experimental cutoff diameters with the theoretical values, we can obtain an empirical factor K to adjust the theoretical values.

Integrating the particle radial velocity and the residence time in the 2 complete turns, the particle total migration distance (Δr) in the vane section is obtained. The particle collection efficiency is then calculated as in Eq. (3.9). By setting $\eta=0.5$ in Eq. (3.9), the theoretical cutoff aerodynamic diameter, $D_{pa50,theo}$, can be derived as

$$D_{pa50,theo} = \frac{0.11\mu(B-w)(r_{max}^2 - r_{min}^2)(r_{max} - r_{min})}{\rho_{p0}\lambda_0 r_{min} P_{760}^2} \times A, \quad (4.4)$$

where $A = P_{in} \times P_{out} / Q_0$, which is the important operating parameter of the cyclone as described earlier.

The collection efficiencies of liquid OA particles at 5 different operation conditions are

shown in Fig. 4.7 as described in the previous section. The comparison of experimental cutoff diameters at different inlet pressures with the numerical values and the theoretical values by Eq. (3.24) is shown in Table 4.1. As expected, the theoretical values are smaller than the experimental results. Therefore, an empirical factor K , which is defined as the ratio of the experimental cutoff size to the theoretical value, is suggested to adjust the theoretical cutoff size. In Table 1, K is shown to be relatively constant with the average and standard deviation of 1.4 and 0.126, respectively. That is, the semi-empirical cutoff aerodynamic diameter can be rewritten as

$$D_{pa50} = 1.4 D_{pa50,theo} \quad (4.5)$$

$$= \frac{0.154\mu(B-w)(r_{\max}^2 - r_{\min}^2)(r_{\max} - r_{\min})}{\rho_{p0}\lambda_0 r_{\min} P_{760}^2} \times A.$$

The above semi-empirical equation is easy to use and is able to predict the cutoff aerodynamic diameter accurately within 9% of error.

If the collection efficiencies are plotted against $\sqrt{St/St_{50}}$, all the experimental data of five different conditions for OA particles are collapsed into a single curve as shown in Fig. 4.12. In the figure, St is defined as

$$St = \frac{\tau \bar{V}_t}{r_{\max} - r_{\min}} \quad (4.6)$$

and St_{50} corresponds to St at 50 % collection efficiency. The slip correction factor used to calculate the particle relaxation time (see Eq. (3.7)) is given as

$$C(D_{pa}) = \frac{1.695 P_{760} \lambda_0}{\sqrt{P_{in} P_{out}} D_{pa} / 2}. \quad (4.7)$$

$\sqrt{P_{in} P_{out}}$ is used in this study as the average pressure on which many other parameters depend.

Combing Eqs. (3.13), (3.15), (4.2) and (4.7), St in Eq. (4.6) is rearranged as

$$St = \frac{0.377 r_{\min} \lambda_0 \rho_{p0} P_{760}^2}{\mu (r_{\max} - r_{\min}) (r_{\max}^2 - r_{\min}^2) (B - w) A} \times D_{pa}. \quad (4.8)$$

It is observed in Fig. 4.12 that all experimental data of particle collection efficiency almost fall on a unique curve, which can be fitted by the following Boltzmann function as

$$Y = 101.4 - \frac{82.5}{1 + e^{(X-1.08)/0.15}}, \quad X < 1.7, \quad (4.9)$$



where Y and X are collection efficiency ($\eta(\%)$) and $\sqrt{St / St_{50}}$, respectively.

Replacing D_{pa} in Eq. (4.8) by the semi-empirical cutoff aerodynamic diameter, D_{pa50} of Eq. (4.5), the semi-empirical $\sqrt{St_{50}^*}$ can be calculated as

$$\sqrt{St_{50}^*} = \sqrt{\frac{0.377 r_{\min} \lambda_0 \rho_{p0} P_{760}^2}{\mu (r_{\max} - r_{\min}) (r_{\max}^2 - r_{\min}^2) (B - w) A} \times D_{pa50}}. \quad (4.10)$$

Table 4.3 Cutoff aerodynamic diameter at different operating conditions, liquid oleic acid (OA) particles.

Q_o (slpm)	0.351 Re=4.9	0.455 Re=6.4	0.566 Re=8.0	0.566 Re=8.0	0.455 Re=6.4
P_{in} (Torr)	4.31	5.43	6.77	7.00	6.00
P_{out} (Torr)	1.46	1.85	2.19	2.97	3.27
$A=P_{in} \times P_{out}/Q_o$	17.93	22.08	26.19	36.73	43.12
Exp. D_{pa50} (nm)	21.69	23.14	25.58	34.71	46.25
Num _{parab} D_{pa50} (nm)	20.4	23.3	25.21	31.2	39.8
Num _{plug} D_{pa50} (nm)	18.1	20.2	23.6	30.6	34.3
Theo. D_{pa50} (nm), Eq (4.5)	13.2	16.5	19.3	27.1	31.8
K (Exp./Theo.)	1.64	1.4	1.33	1.28	1.45

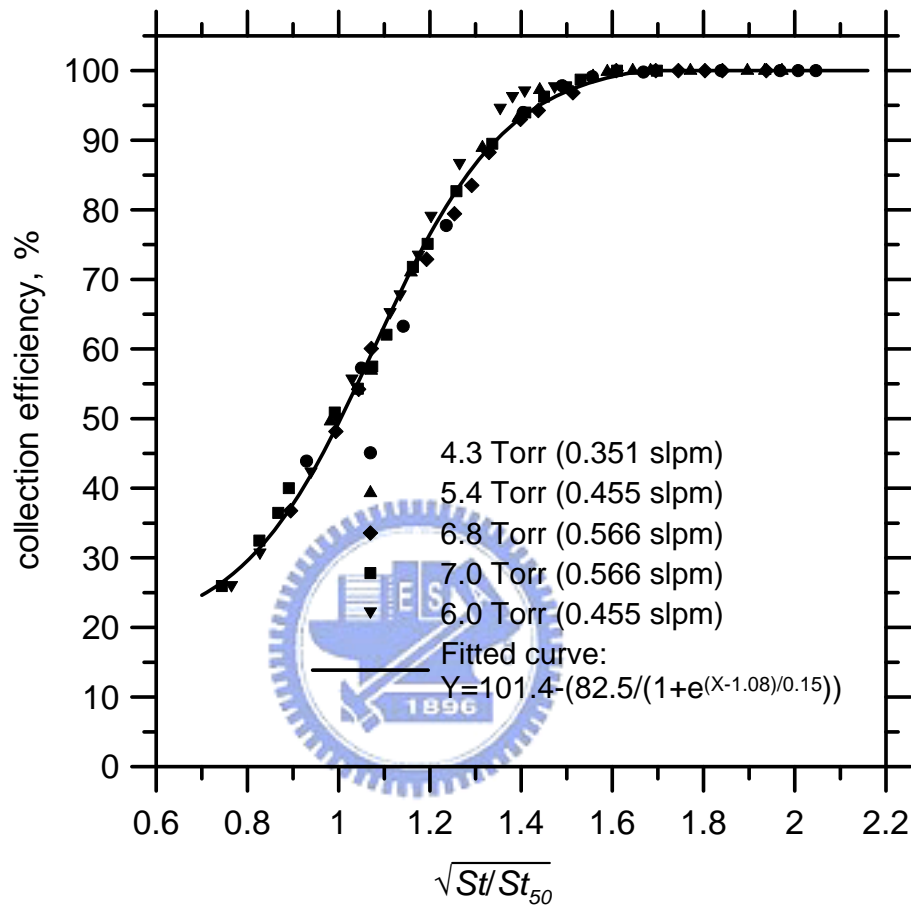
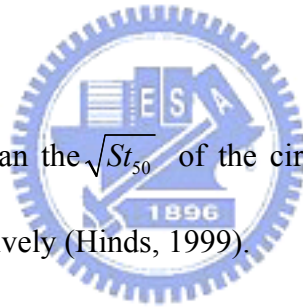


Figure 4.12 Collection efficiencies versus $\sqrt{St/St_{50}}$ for OA particles at different inlet pressures and flow rates.

Substituting Eq. (4.5) into Eq. (4.10), $\sqrt{St_{50}^*}$ is found to be a fixed value of 0.241. The experimental collection efficiency versus \sqrt{St} (calculated from Eq. (4.8)) for all five test conditions was plotted (not shown here), and the experimental $\sqrt{St_{50}}$ was calculated to be 0.256, 0.240, 0.222, 0.226 and 0.240 for $P_{in} = 4.3, 5.4, 6.8, 7.0$ and 6.0 Torr, respectively. The difference between the experimental $\sqrt{St_{50}}$ and the semi-empirical $\sqrt{St_{50}^*}$, or 0.241, is -6.2, 0.4, 7.9, 1.5 and 0.4 % for $P_{in} = 4.3, 5.4, 6.8, 7.0$ and 6.0 Torr, respectively. That is, for the present axial flow cyclone for removing nanoparticles, the design value for the square root of the cutoff Stokes number is

$$\sqrt{St_{50}^*} = 0.241. \quad (4.11)$$

This value is much smaller than the $\sqrt{St_{50}}$ of the circular jet and rectangular jet impactor, which is 0.49 and 0.77, respectively (Hinds, 1999).



4.4 Results of Brownian Dynamic simulation for particle collection efficiency

4.4.1 Comparison of simulated collection efficiency with present experimental data

For different operation conditions, Table 4.2 summarizes the comparison of simulated cutoff aerodynamic diameter with the experimental data. The agreement between the experimental data and the numerical results is observed in the cutoff aerodynamic diameter, which is from about 20 nm to 50 nm for the operating conditions listed in Table 4.2. The maximum deviation is 6.2 % for $Q_0=0.566$ slpm and $P_{in}=6.77$ Torr. For other conditions, the deviation is less than 4 %.

The current experimental particle collection efficiencies and numerical results of BD simulation are shown in Figs. 4.13 (a) and (b) for the operating conditions of $P_{in} = 6.0$ and 7.0 Torr, and in Fig. 4.14 for $P_{in} = 4.31, 5.43,$ and 6.77 Torr, respectively.

In Figs. 4.13 (a) and (b), the collection efficiency curves with and without considering Brownian diffusion are compared for $P_{in} = 6$ and 7.0 Torr, respectively. When Brownian diffusion is considered, the present numerical results agree with the experimental collection efficiencies very well for both inlet pressures in the whole range of diameters studied. Without considering Brownian diffusion, the numerical collection efficiencies still match very well with the experimental data for particles greater than the cutoff diameter; however they are lower than the experimental data when particles are smaller than the cutoff diameter. The largest difference of 12.5% occurs at the smallest particle diameter of 27 nm (Fig. 4.13 (a)). The increase in the diffusional deposition was found to occur mainly in the chamber after the vane section when the gas expands and slows down, and there was no increase of the collection efficiency due to short residence time of particles in the vane section. For particles greater than the cutoff size, the centrifugal force dominates and whether or not Brownian diffusion is considered does not make any difference in the collection efficiency curves. For the cutoff diameter, simulation considering Brownian diffusion results in smaller and more-

accurate results than not considering Brownian diffusion when $P_{in}=6$ and with 7 Torr. Table 4.1 also shows the cutoff diameter of 36.98 and 50.03 nm (or 1.0 and 0.6% error) with consideration of Brownian diffusion, and 37.35 and 50.92 nm (or 1.9 and 2.3 % error) without considering Brownian diffusion.

Fig. 4.14 shows that all numerical results agree with the experimental collection efficiencies very well in the whole range of the cutoff aerodynamic diameter, when Brownian diffusion is considered. The error in the numerical cutoff aerodynamic is 3.2, 1.1, and 4.1 %, for $P_{in} = 4.3, 5.4,$ and 6.77 Torr, respectively. Neglecting Brownian diffusion in the simulation, particle collection efficiencies are similar to those in Fig. 4.14, and the error in the cutoff aerodynamic diameter becomes slightly larger. The error is 3.8, 1.9, and 6.2 %, for $P_{in} = 4.31, 5.43,$ and 6.77 Torr, respectively. These comparisons are also shown in Table 2. In Fig. 4.14, few data points exist for particles below the cutoff aerodynamic diameter, since particle concentration becomes too low to obtain accurate efficiency data. If such data were available, Brownian diffusion would be expected to increase the collection efficiency for particles below the cutoff aerodynamic diameter similar to Fig. 4.13.

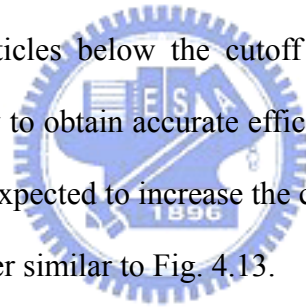


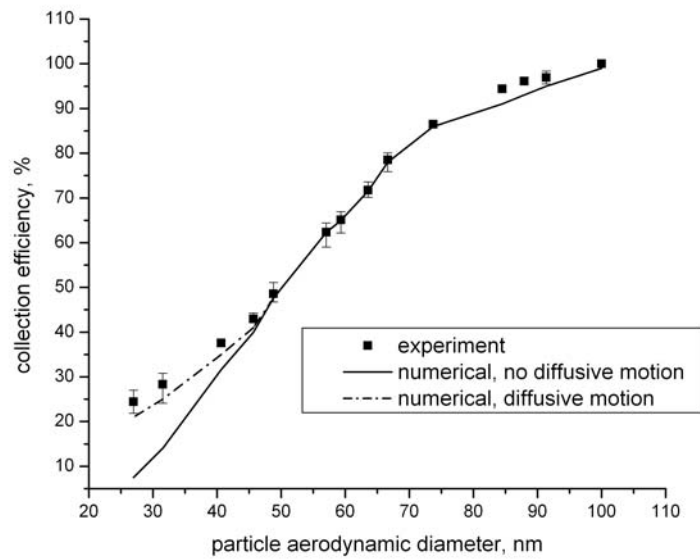
Table 4.4 Cutoff aerodynamic diameter for different operating conditions.

$Q_0(\text{slpm})$	0.351	0.455	0.566	0.566	0.455
$P_{in}(\text{Torr})$	4.31	5.43	6.77	7.00	6.00
$Dp_{50num}(\text{nm})$	22.39	23.40	26.65	36.98	50.03
$Dp_{50num}(\text{nm})^*$	22.54	23.59	27.27	37.35	50.92
$Dp_{50exp}(\text{nm})$	21.69	23.14	25.58	36.65	49.75

*: Brownian diffusion is neglected



(a)



(b)

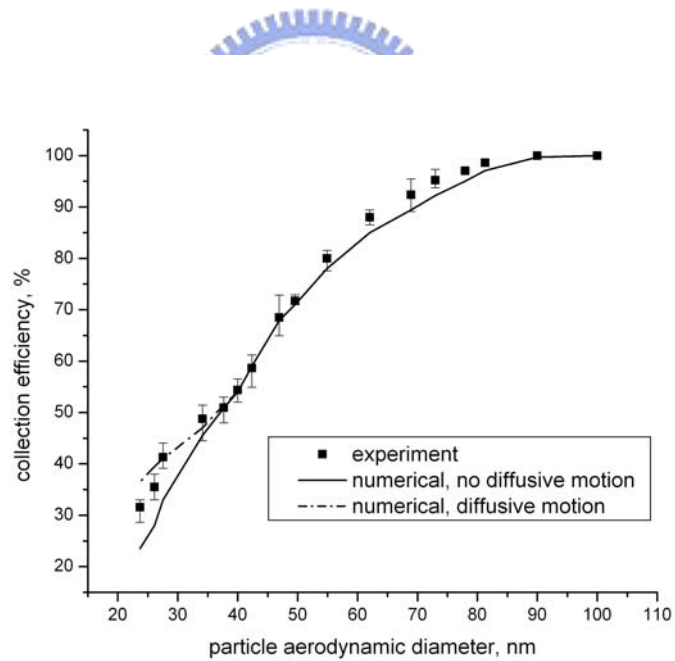


Figure 4.13 Comparison of numerical collection efficiencies and present experimental data, (a)

$P_{in}=6.0$ Torr; (b) $P_{in}=7.0$ Torr.

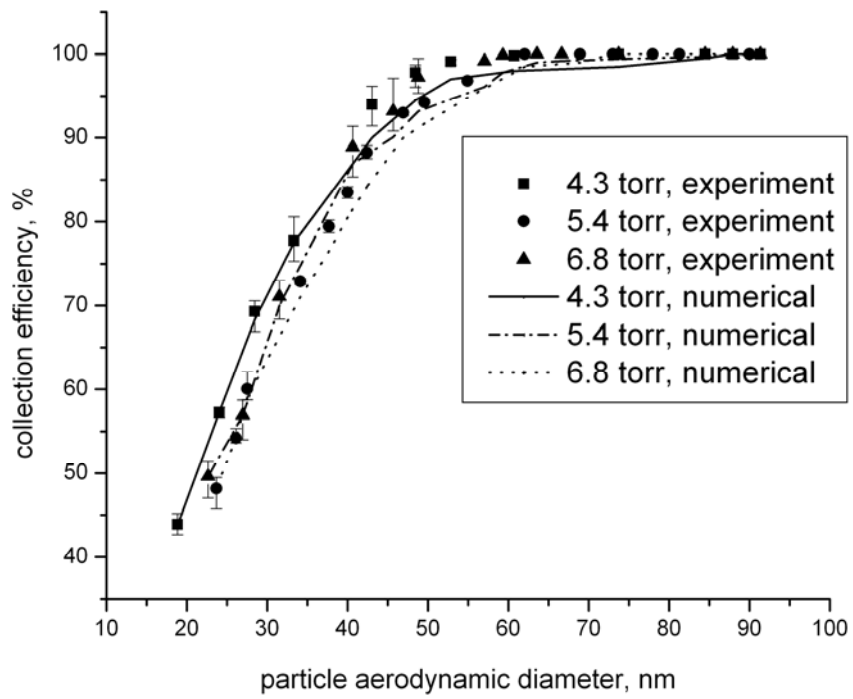


Figure 4.14 Comparison of numerical collection efficiencies and present experimental data, $P_{in}=4.3, 5.4, 6.8$ Torr.

4.4.2 Comparison of simulated collection efficiency with the results of Hsu et al. (2005)

Figs. 4.15 (a) and (b) show the comparison of the numerical results of the present BD calculations with the experimental results obtained by Hsu et al. (2005), for $P_{out}=6.5$, and $P_{out}=4.8$ Torr, respectively. The flow rate in both figures is 0.455 slpm. It can be seen that the current BD simulation predicts the collection efficiency reasonably well for both small and large particles in both cases.

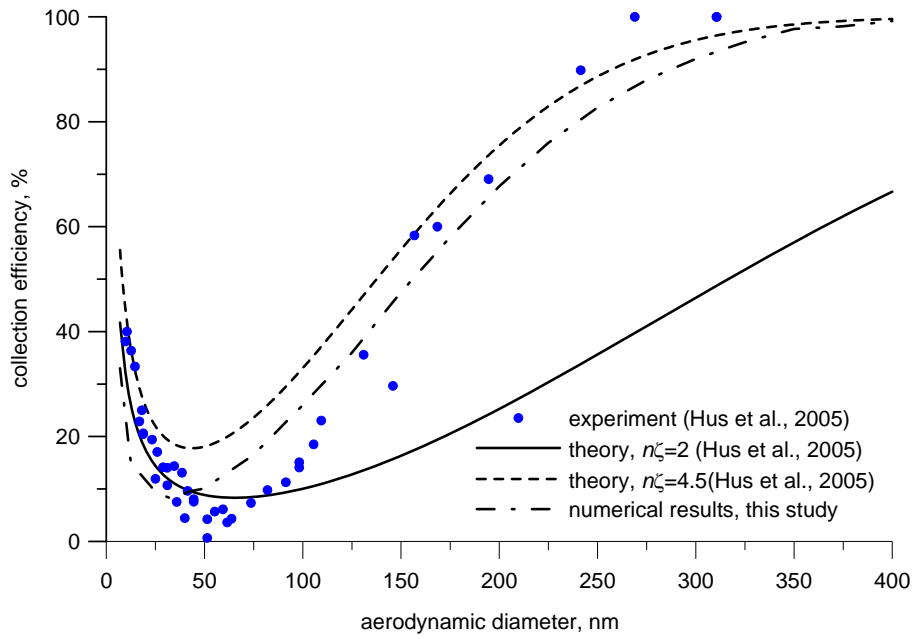
In comparison, the Hsu et al. (2005) theoretical equation ($n\zeta=4.5$), Eq. (3.13), is less accurate than the simulation. The maximum error occurs near the minimum collection efficiency in Eq. (3.13), which overestimates the collection efficiency compared to current BD simulation. This overestimation is suspected to be due to the simplified plug-flow assumption, and to assuming three rotations in the vane and the extra 1.5 rotation in the chamber. To investigate this matter further, we assumed two rotations of the flow in the vane section and no rotations in the chamber, or setting $n\zeta = 2$, and used the Hsu et al. (2005) model to re-calculate the theoretical collection efficiency. Results are also shown in Figs. 4.15 (a) and (b). From Fig. 4.15 (a), it is seen that assuming $n\zeta=2$ will result in theoretical collection efficiencies that match the experimental data slightly better than the original assumption of $n\zeta=4.5$. However, there are no experimental data to compare the theories for particles larger than 50 nm. In Fig. 4.15 (b), assuming $n\zeta=2$ results in better agreement than the original assumption of $n\zeta=4.5$ for particles less than 100 nm, but substantial disagreement exists for particles greater than 100 nm for the assumption of $n\zeta=2$. That is, not only the number of flow rotations must be accurate, but accurate flow and pressure profiles are also critical for obtaining accurate theoretical particle collection efficiency. The agreement of the calculated collection efficiencies of Hsu et al. (2005) and the experimental data seen in Fig. 7 based on $n\zeta = 4.5$ is just fortuitous.

In Fig. 14.5, the collection efficiency due to diffusional deposition of small nanoparticles

increases with decreasing diameter when the diameter is smaller than about 40 to 60 nm, which corresponds to the minimum collection efficiency. The current BD simulation shows such diffusional deposition mainly occurs in the chamber after the vane section, not in the vane section. For example, the total numerical collection efficiency is 18.3 % for 9.8 nm nanoparticles in Fig. 4.15 (a), in which 14.9 % occurs in the chamber after the vane, and only 2.1 % in the first turn of the vane and 1.3 % in the vane between 1 and 1.5 turns. This results can explain that large differences (13.9 %) were occurred of the cutoff size between the previously experimental data and the theoretical calculations (paraboloid assumption, $P_{in}=6$ Torr). In this condition, flow has longer residence time in the chamber and the theoretical methods miss the diffusion loss in it.

In Fig. 4.15 (b), the total numerical collection efficiency is 18.5 % for 11.34 nm nanoparticles, including 15.5, 1.8 and 1.2 % in the chamber after the vane in the first turn, and the vane between 1 to 1.5 turns, respectively. The diffusional deposition is small in the cyclone's vane section as the flow residence time is usually small (on the order of 0.003 sec) for the cyclone operating in vacuum conditions. In addition to the vane section, the theoretical prediction of particle deposition in the vane chamber is difficult due to the complexity of the flow field in it. The only way to calculate the collection efficiency of nanoparticles accurately is by the numerical flow and particle simulation, such as the BD simulation in this study.

(a)



(b)

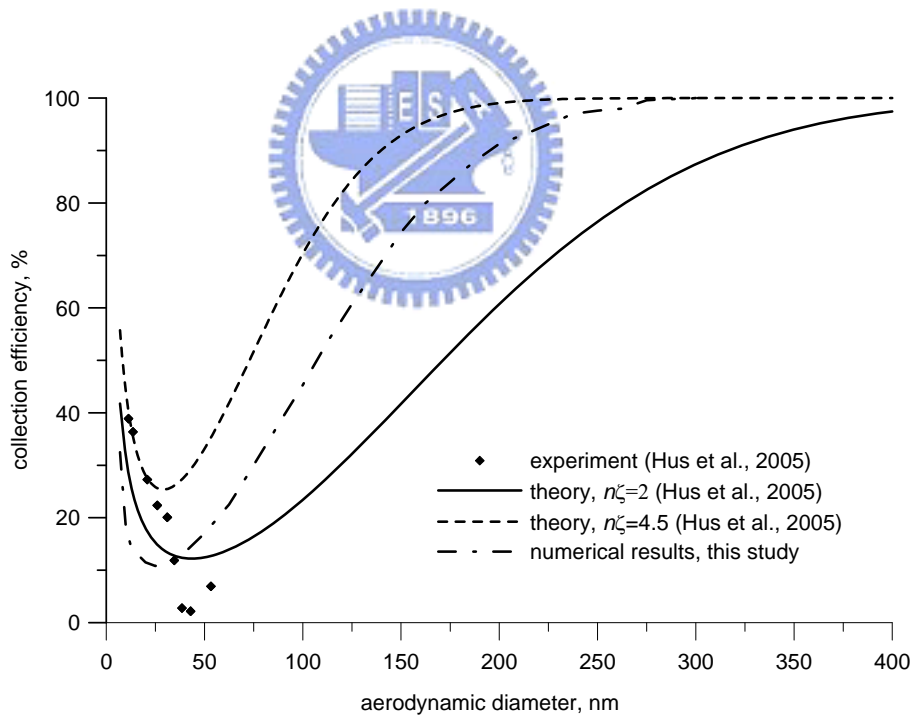


Figure 4.15 Comparison of the present numerical collection efficiencies with the experimental data and the theory by Hsu et al. (2005), $Q_i=0.455$ slpm (a) $P_{out}=6.5$ Torr, (b) $P_{out}=4.8$ Torr

CHAPTER 5

CONCLUSIONS AND RECOMMENDATIONS

5.1 Conclusions

In this study, a low pressure cyclonic separator for nanoparticle removal was designed and tested. The device includes a critical orifice and an axial flow cyclone connected downstream of the orifice. The orifice was used to reduce the pressure of the cyclone. At reduced pressure, particle slip correction factor is increased and particle drag force decreased by a significant amount resulting in an increasing collection efficiency of nanoparticles.

First, this study investigated particle loss in the orifice and the method to reduce the loss. The loss of particles in different parts of the orifice assembly was determined experimentally and numerically. Particle loss in the inlet tube and the back surface of the orifice were not found, however, significant loss could occur on the front surface of the orifice and the tube wall after the orifice.

At $P_{od}= 260$ Torr, the experimental particle loss on the orifice plate for O'Keefe E-9 orifice is 0.2, 0.97, 6.31 and 12.35% for particles of 2, 2.8, 6.5 and 10 μm in aerodynamic diameter. The simulated results show good agreement with the data with a maximum deviation within 4.5 %. Modifying the present orifice plate to have a contraction half-angle below 30° is expected to reduce the inertial impaction loss below 5% for particle as large as 15 μm in aerodynamic diameter.

At $P_{od}= 260$ Torr, the experimental particle loss in the tube after the orifice for O'Keefe E-9 is 82.5, 83.2, 72.0 and 49.1% for particle sizes of 2, 2.8, 6.5 and 10 μm , respectively, in aerodynamic diameter. The simulated results are also in good agreement with the data with a maximum deviation within 10.5 %. If the outlet tube diameter is increase from 6.2 to 25 mm, the maximum theoretical loss of the 2.8 μm particle is reduced from 78.3% to 38.3%. For

particles below 100 nm, particle loss in the tube after the orifice will be decreased from 50 to nearly 0% when the orifice downstream pressure 4 to 6 Torr if the inner diameter of the outlet tube is increased from 6.2 to 25 mm.

The axial flow cyclone of Tsai et al. (2004) was further tested for the collection efficiencies of solid NaCl and liquid OA nanoparticles in the diameter from 12 to 100 nm at low-pressure conditions (4.3, 5.4, 6.0, 6.8, and 7.0 Torr). The objective was to find whether solid particle bounce would influence the collection efficiencies. The axial flow cyclone was shown to be able to remove NaCl and OA nanoparticles below 50 nm efficiently. The smallest cutoff aerodynamic diameters of OA and NaCl particles were found to be 21.7 (4.3 Torr, 0.351 slpm) and 21.2 (5.4 Torr, 0.454 slpm), respectively. Differences in the collection efficiencies of liquid and solid particles were within 10% indicating that the effect of solid particle bounce on the collection efficiency was not very obvious. The test for the solid particle loading in the cyclone further indicated a soiled cyclone wall did not change the collection efficiency too much (<10%).

In order to predict the collection efficiency and cutoff diameter accurately, a 3-D numerical simulation was conducted to obtain the pressure distribution and gas velocity fields in the cyclone. Results showed that the tangential flow developed quickly into paraboloid flow profile near the end of the first turn of the vane section. Total migration distance was calculated based on the local tangential flow velocity and pressure to obtain the numerical collection efficiency.

The comparison of the experimental particle collection efficiencies and cutoff diameters with the numerical simulations showed that the paraboloid tangential flow assumption yielded better results than the plug flow assumption, with the maximum error of 15 % for the collection efficiencies and 13.9 % for the cutoff diameters, respectively.

Based on the simulated pressure and tangential flow fields, a modified theoretical method from Tsai et al. (2004) was proposed. The semi-empirical equations were then

developed to predict the cutoff aerodynamic diameter and the cutoff Stokes number accurately within 9% and 8 % of error, respectively. Based on the semi-empirical cutoff aerodynamic diameter, the design value of the square root of the cutoff Stokes number, $\sqrt{St_{50}^*}$, was calculated and found to be a constant value of 0.241.

BD simulation combining with the CFD code for calculating particle trajectories in the cyclone with considering both centrifugal force and Brownian diffusion of particles was studied. The simulated results agree with the experimental data very well. From the simulated results, it was found the diffusional deposition mainly occurs in the chamber after the vane section when the gas expands and slows down, and there was no increase of the collection efficiency due to short residence time of particles in the vane section. Because the theoretical prediction of particle deposition in the vane chamber is difficult due to the complexity of the flow field in it, the only way to calculate the collection efficiency of nanoparticles accurately is by the numerical flow and particle simulation, such as the BD simulation in this study.

The low pressure cyclone separator developed in this study can remove nanoparticles efficiently. The derived semi-empirical equation of cutoff aerodynamic diameter and the results of BD simulation can facilitate the design of the low pressure cyclonic separator to classify nanopowders below a certain diameter, to remove toxic nanoparticles from the vacuum exhaust of process chambers commonly used in high-tech industries, and can be used for nanoparticle sampling.

5.2 Recommendations

- (1) Testing the low pressure cyclonic separator at high particle concentration is important for future application of the separator as a dust control device.
- (2) Reducing the pressure drop of the separator will be beneficial to the development of the separator as a nanoparticle sampling device.

(3) Present results can be used to design an orifice with high transmission efficiency. It is worthwhile to calculate the particle loss in the orifice using BD simulation considering both impaction and diffusion mechanisms simultaneously.



REFERENCES

- Barth, W. (1956) Berechnung und Auslegung von Zyklonabscheidern. *Brennst. Wärme Kraft*, **8**, 1-9.
- Biswas, P. and R. J. Flagan (1988) Particle trap impactor. *J. Aerosol Sci.*, **19**, 113-121.
- Blachman, M. W. and M. Lippmann. (1974) Performance characteristics of the multicyclone aerosol sampler. *Am. Ind. Hyg. Assoc. J.*, **35**, 311-326.
- Boysan, F., B. C. R. Ewan, J. Swithenbank and W. H Ayers. (1983) Experimental and theoretical studies of cyclone separator aerodynamics. *ICHEME. Symp. Series*, **69**, 305-320.
- Chandrasekhar, S. (1943) Stochastic problems in physics and astronomy. *Review of Modern Physics*, **15**, 1-89.
- Das, Rishiraj and Denis J. Phares. (2004) Expansion of an ultrafine aerosol through a thin-plate orifice. *J. Aerosol. Sci.*, **35**, 1091-1103.
- Dietz, P. W. (1981) Collection efficiency of cyclone separators. *AIChE J.*, **27**, 888-892.
- Chen, D.-R., and D. Y. H. Pui. (1995) Numerical and experimental studies of particle deposition in a tube with a conical contraction—Laminar flow regime. *J. Aerosol. Sci.*, **26**, 563-574.
- Harwood, R. and M. Slack. (2002) CFD analysis of a cyclone. *QNET-CFD Network Newsletter*. **1**, 25-27.
- Hinds, W. C. (1999) Aerosol technology. New York: John Wiley & Sons. Inc. p126.
- Hoekstra, A. J., J. J. Derksen and H. E. A. Van Den Akker. (1999) An experimental and

- numerical study of turbulent swirling flow in gas cyclones. *Chem. Eng. Sci.*, **54**, 2055-2065.
- Hsu, Y. D., H. M. Chein, T. M. Chen, and C. J. Tsai. (2005) Axial flow cyclone for segregation and collection of ultrafine particle: Theoretical and experimental study. *Environ. Sci. Technol.*, **39**, 1299-1308.
- Iozia, D. L. and D. Leith. (1990) The logistic function and cyclone fractional efficiency. *Aerosol Sci. Technol.*, **12**, 598-606.
- Issa, R. I. (1986) Solution of the implicitly discretised fluid flow equations by operator-splitting. *J Comp. Phys.*, **62**, 40-65
- Kanaoka, C., H. Emi, and B. Tarthapanichakoon. (1983) Convective diffusional deposition and collection efficiency of aerosol on a dust loaded fiber. *AIChE J.* **29**, 895-902.
- Kao, K. Y. and C. J. Tsai. (2001) On the theory of particle collection efficiency of cyclones. *Aerosol Air Qual. Res.*, **1**, 47-56.
- Kenny, L. C., Gussman, R., and M. Meyer (2000) Development of a sharp-cut cyclone for ambient aerosol monitoring applications. *Aerosol Sci. Technol.*, **32**, 338-358.
- Lapple, C. E. (1950) Gravity and centrifugal separation. *Ind. Hyg. Quart.*, **11**, 40-48.
- Lee, J. K., K. L. Rubow, D. Y. H. Pui and B. Y. H. Liu. (1993) Design and performance evaluation of a pressure-reducing device for aerosol sampling from high-purity gases. *Aerosol. Sci. Technol.*, **19**, 215-226.
- Lee, J. W., M. Y. Yi and S. M. Lee. (2003) Inertial focusing of particles with an aerodynamic lens in the atmospheric pressure range. *J. Aerosol. Sci.*, **34**, 211-224.
- Leith, D., and W. Licht. (1972) The collection efficiency of cyclone type particle collectors: a

- new theoretical approach. *AIChE Symp. Ser.*, **126**, 196-206.
- Li, E. and Wang, Y. (1989). A new collection theory of cyclone separators. *AIChE J.*, **35**, 666-669.
- Librizzi, J. and R. R. Manna. (1983) Microelectronics manufacturing and testing. **6**, 46.
- Liu, B. Y. H. and K. L. Rubow. (1984) A new axial flow cascade cyclone for size characterization of airborne particulate matter. In: *Aerosols* (Liu, B. Y. H., D. Y. H. Pui and J. Ed. Fissan). pp. 115-118, Elsevier, Amsterdam.
- Maynard, A. D. (2000) A simple model of axial flow cyclone performance under laminar flow conditions. *J. Aerosol Sci.*, **31**, 151-167.
- McMahon, R. (1998) Microelectronics manufacturing and testing. **12**, 8.
- Muyschondt, A., A. R. McFarland and N. K. Anand. (1996) Deposition of aerosol particles in contraction fittings. *Aerosol. Sci. Technol.*, **24**, 205-216.
- Patankar, S. V. (1980) Numerical heat transfer and fluid flow. Washington: Hemisphere Publishing Co.
- Peters, T. M., and R. W. Vanderpool. (1996) Modification and evaluation of the WINS impactor, *R. T. I. Report* No. 6360-011.
- Podgórski, A. (2002) *On the transport, deposition and filtration of aerosol particles in fibrous filters: selected problems*, Oficyna Wydawnicza Politechniki Warszawskiej, Warsaw.
- Pui, D. Y. H., Y. Ye and B. Y. H. Liu. (1988) in *Proc. 9th Int. Symp. on Contamination Control*, Los Angeles, CA, September, pp. 26-30.
- Ramarao, B., C. Tien and S. Mohan. (1994) Calculation of single fiber efficiencies for interception and impaction with superposed Brownian motion. *J. Aerosol. Sci.*, **25**, 295-

313.

Sato, S., D. R. Chen and D. Y. H. Pui. (2002) Particle transport at low pressure: Particle deposition in a tube with an abrupt contraction. *J. Aerosol. Sci.*, **33**, 659-671.

Schmidt, S. and F. Thiele. (2002) Comparison of numerical methods applied to the flow over wall-mounted cubes. *Inter. J. Heat & Fluid Flow*. **23**, 330-339.

Schmidt, S., H.M. Blackburn, M. Rudman and I. Sutalo. (2003) Simulation of turbulent flow in a cyclonic separator. 3rd International conference on CFD in the Minerals and Process Industries CSIRO, Melbourne, Australia, 10-12 December 2, pp. 365-369.

Tsai, C. J., H. G. Shiau, K. C. Lin and T. S. Shih. (1999) Effect of deposited particles and particle charge on the penetration of small sampling cyclones. *J. Aerosol Sci.*, **30**, 313-323.

Tsai, C. J. and T. I. Lin. (2000) Particle collection efficiency of different impactor designs. *Sep. Sci. Technol.*, **35**, 2639-2650.

Tsai, C. J. and Y. H. Cheng. (1995) Solid particle collection characteristics on impaction surfaces of different designs. *Aerosol Sci. Technol.*, **23**, 96-106.

USEPA. (1997) Ambient Air Monitoring Reference and Equivalent Methods. United States Environmental Protection Agency, Federal Register 40 CFR Parts 50.

Vanderpool, R. W., Lundgren, D. A., Kerch, P. E. (1990) Design and calibration of an in-stack low-pressure impactor. *Aerosol Sci. Technol.*, **12**, 215-224.

Vaughan, N. P. (1988) Construction and testing of an axial flow cyclone pre-separator. *J. Aerosol Sci.*, **19**, 295-305.

Weiss, Z., P. Martinec and J. Vitek. (1987) Vlastnosti dulnibo prachu a zaklady protiprasne techniky, Prague, SNTL.

Xiang, R. B. and K. W. Lee. (2004) The flow pattern in cyclones with different cone dimensions and its effect on separation efficiency. *Abstract, EAC 2004*, Budapest, Hungary, Sep. 6-10, pp. 289-290.

Ye, Y., and D. Y. H. Pui. (1990) Particle deposition in a tube with an abrupt contraction. *J. Aerosol. Sci.*, **21**, 29–40.

Zhu, Y. and K. W. Lee. (1999) Experimental study on small cyclones operating at high flowrates. *J. Aerosol Sci.*, **30**, 1303-1315.

